Induced unconventional superconductivity on the surface states of Bi_2Te_3 topological insulator

Authors:

S. Charpentier[1†], L. Galletti[1†], G. Kunakova[1,2], R. Arpaia[1], Y. Song[1,3], R. Baghdadi[1], S. M. Wang[1,3], A. Kalaboukhov[1], E. Olsson[4], F. Tafuri[5], D. Golubev[6], J. Linder[7], T. Bauch[1] and F. Lombardi[1*]

Affiliations:

[1]Department of Microtechnology and Nanoscience, Chalmers University of Technology, SE-41296 Göteborg, Sweden

[2]Institute of Chemical Physics, University of Latvia, 19 Raina Blvd., LV-1586, Riga, Latvia

[3]Shanghai Institute of Microsystem and Information Technology, Chinese Academy of Sciences, 865 Changning Road, Shanghai CN-200050, China

[4]Department of Applied Physics, Chalmers University of Technology, SE-41296 Göteborg, Sweden

[5]Dipartimento di Ingegneria dell'Informazione, Seconda Università di Napoli, IT-81031 Aversa (CE), Italy and CNR-SPIN

[6]Department of Applied Physics, Aalto University School of Science, P.O. Box 13500, FI-00076 Aalto, Finland

[7]Department of Physics, Norwegian University of Science and Technology, N-7491 Trondheim, Norway

*Correspondence to: floriana.lombardi@chalmers.se

† These authors equally contributed to the work

Abstract:

Topological superconductivity is central to a variety of novel phenomena involving the interplay between topologically ordered phases and broken-symmetry states. The key ingredient is an unconventional order parameter (OP), with an orbital component containing a chiral p_x+ip_y wave term. Here we present phase-sensitive measurements, based on the quantum interference in nanoscale Josephson junctions, realized by using Bi_2Te_3 topological insulator. We demonstrate that the induced superconductivity is unconventional and consistent with a sign-changing order parameter, such as a chiral p_x+ip_y component. The magnetic field pattern of the junctions shows a dip at zero externally applied magnetic field, which is an incontrovertible signature of the simultaneous existence of 0 and π coupling within the junction, inherent to a non trivial OP phase. The nano-textured morphology of the Bi_2Te_3 flakes, and the dramatic role played by thermal strain are the surprising key factors for the display of an unconventional induced OP.

Introduction:

The notion of superconducting materials with fully gapped order parameters, but that still support topologically protected surface states[1-5], including Majorana bound states[2,3], are currently subject to much attention. Such systems intertwine two key paradigms in condensed matter physics, namely spontaneous symmetry breaking and topology, which has been predicted to cause unusual quantum phenomena with even direct analogies to concepts in high-energy physics, such as axion couplings[6]. This novel physics has been recently predicted to occur also in systems where the superconducting phenomenon involves topological Dirac electrons and it can be induced by the proximity with a conventional superconductor.

Heterostructures involving a conventional superconductor (S) and an exotic conductor, represented by the surface of a 3D topological insulator[7-11] (TI) and the edge states of two-dimensional quantum wells[12,13], are ideal systems to emulate topological superconductivity. In the pioneering work by Fu and Kane[1] the superconductivity induced in the surface states of a 3D TI is described, in a basis where the operators acquire a phase factor, by an OP which resembles a spinless chiral p_x+ip_y (p) but does not break time reversal symmetry. In a subsequent work, Tkatchov at al.[14] have derived, this time in a canonical operator basis, that the induced superconductivity has an orbital term of the type p+s-wave with the p part, consisting of conventional chiral p_x+ip_y and p_x-ip_y, that sums up with the s-wave term through Pauli matrices to form the total superconducting order parameter.

It is clear that the first step that must be taken to unveil the rich variety of the predicted phenomena related to topological superconductivity is to clearly demonstrate the

unconventional nature of the OP, which identifies in a chiral p_x+ip_y (p-wave) orbital term. In compounds like the Sr_2RuO_4 layered perovskite, for example, considered the archetype of a topological superconductor, the existence of a chiral p_x+ip_y wave orbital order, with a nontrivial internal phase, is still not generally accepted[15]**.** The appearance of Majorana fermions and topological quantum computation are fundamentally encoded in the properties of such p-wave superconductivity.

Josephson interferometry emerges as a crucial tool to show key features of the superconductivity involving topological Dirac electrons, as for instance supercurrents induced in the helical edge states of HgTe/HgCdTe[12] and InAs/GaSb[13] 2D TI quantum wells. The helical metallic surface states of 3D TI, probed by Josephson interferometry have shown, up to now, a mostly conventional induced superconductivity. Here the Josephson transport has been demonstrated to be ballistic[8,10] and uniquely associated with the helical surface states[16] which rules out a contribution from the disordered bulk[8,10]. However no other signatures have been observed. The reports on a skewed Josephson current phase relation could not be clearly discriminated if due to a conventional high transparency barrier in S-3DTI-S junctions[17] or to the peculiar bound state spectrum of the surface helical metal[11,14] possibly hosting Majorana fermions.

Our experiment is a decisive step along this line. We have realized hybrid devices based on a 3D TI, where the nanostructured morphology of the topological insulator flakes makes the measurement of the Josephson effect sensitive to the interface unconventional order parameter symmetry. By using the same path and notions previously employed to prove the d-wave OP in high critical temperature superconductors[18,19] (HTS) we have measured an unconventional magnetic field pattern of the Josephson current, with a dip at zero magnetic

field. We demonstrate that this is the incontrovertible code of a Cooper pair tunneling process probing an OP with a non-trivial internal phase.

Results:

Unconventional magnetic field patterns in Al-Bi_2Te_3-Al Josephson junctions.

Al-3DTI-Al Josephson junctions (Fig. 1a) have been realized using Bi_2Te_3 flakes from epitaxial thin films. By varying the interface transparency D, from a value close to 1 to the tunneling limit ($D \ll 1$) we have been able to show that the surface states of Bi_2Te_3 host an induced OP with a non trivial phase compatible with a chiral p-wave. Figure 1b shows the nanostructured morphology of the flakes. We observe characteristic pyramidal domains (see Methods section) with a prevailing single domain, which points towards thin films without twin boundaries[20].

Figure 1c shows the current voltage characteristic (IVC) of a typical junction at the first cool down, measured at base temperature of 20 mK in a dilution refrigerator. The curve presents 50% hysteresis and a large excess current I_{exc}, defined as the extrapolation at zero voltage of the IVC above the Al gap, Δ_{Al}. This value can be higher than the Josephson current for high transparent interfaces[21] as we generally find for our devices. We will assume that the junctions can be assimilated to S'INIS' structures where S' is the effective fully gapped *p+s*-wave superconductor[14], N is the Bi_2Te_3 Dirac metal channel and I the interface barrier (see Fig. 1d). The induced gap in S' will define the maximum $I_C R_N$ product where I_C represents the maximum Josephson current and R_N the normal resistance of the junction. For the IVC of Fig. 1c we get an $I_C R_N \approx 100$ μV indicating an induced gap close to that of the Al[22]. This is further supported by the high value of the transparency D we extract from the IVC.

Specifically from the value $eI_{\mathrm{exc}}R_{\mathrm{N}}/\Delta_{\mathrm{S}'}$, with $\Delta_{\mathrm{S}'} \approx \Delta_{\mathrm{Al}}$, we can extrapolate the value of the barrier transparency $D \cong 0.8$ [21].

Figure 2 shows the magnetic field dependence of the Josephson current for the same junction as in Fig. 1c. We observe an ideal Fraunhofer pattern with clear secondary lobes (cyan circles). From the modulation period $\Delta B = \phi_0/A_{\mathrm{eff}} \approx 2.5$ mT, where ϕ_0 is the superconducting flux quantum, we extract an effective area A_{eff} of 0.75 μm^2. This value is very close (within few %) to the numerically calculated effective area, by assuming a 2π periodic current phase relation (see Supplementary Note 1). This has been verified for several junctions on various chips, which confirms a conventional magnetic field behavior of the devices in agreement with the theoretical predictions[23] and various experimental reports[24], while in contrast with the anomalies stated in earlier works[25].

After thermal cycling (from base temperature to 300 K and back to base temperature) the transport properties of all devices undergo a dramatic change. The critical current of the junctions is, for most devices, reduced by more than two orders of magnitudes (see Fig. 2) while the normal resistance increased by a factor between 1.1 and 6 (see Table 1).

We shall argue that this phenomenology is related to the dramatic role played by strain to tune the interquintuple layers interaction and therefore the topological phase in TIs. First principle calculations[26,27] have shown that the consequence of a tensile strain (out of plane compression) is a shift of the Dirac point closer to the valence band while a compressive strain (out of plane expansion) leads to a gap opening at the Dirac point[26]. Strain is usually generated during the epitaxial growth of the material on the substrate, with lattice parameters different from those of the topological insulator. Recent reports have shown the

tunability of the Dirac point by strain in thin topological crystalline insulator SnTe[28] and at grain boundaries in Bi_2Se_3 thin films[29].

Our experiment is quite different: exfoliated Bi_2Te_3 flakes are transferred to a SiO_2/Si substrate, so a possible strain-related phenomenology cannot be attributed to the growth process. The strain instead is related to the huge difference in the thermal expansion coefficient of Bi_2Te_3 ($\sim 13.4 \times 10^{-6}$ °C^{-1}) and that of the SiO_2/Si substrate (0.5×10^{-6} °C^{-1}/2.4×10^{-6} °C^{-1}). The flake will experience this difference by the clamping to the substrate, through the patterning of the Al electrodes forming a nanometer sized gap junction. During the warming up of the sample the Bi_2Te_3 flake at the nanogap undergoes a compressive strain inducing plastic deformation that leads to a buckling of the Bi_2Te_3 channel forming the nanogap upon a subsequent cool down[30]. Figure 3 shows a SEM picture of a junction after cycling; a typical buckling feature appears in the nanogap (see Supplementary Note 3).

Plastic deformations at the nanochannel can substantially affect the Josephson properties. The opening of a gap at the Dirac node, which can eventually reach the bulk gap[26], works as a tunneling barrier reducing the Josephson current as we observe in our experiment. The physics behind this reduction is that the opening of a gap at the Dirac node causes current-carrying surface states beneath the Al electrodes to become evanescent waves in the TI nanogap region, which thus decay over a shorter distance than in the gapless case and thus reduces the critical current.

For the devices, which undergo the most dramatic changes in the Josephson current, the value of the I_{exc} is zero, signifying a very low transparency. However for these samples the most striking experimental observation is the inverted Josephson magnetic field pattern that

appears after thermal cycling (Fig. 2 (blue points) and Fig. 4a, see also Supplementary Figure 2, and Supplementary Note 2).

Discussion:

Our results are consistent with a proximity-induced superconductivity in the TI surface states compatible with a *p*+*s* OP which contains a chiral *p*-wave term. Let's now focus on the effect of the interface transparency on the chiral *p*-wave part of the *p*+*s* OP. Self-consistent calculations have shown that the transparency of the interface can have a dramatic effect on a chiral p_x+ip_y wave OP. For highly transparent interfaces, both the p_x and p_y component of OP gap are equally suppressed at the interface[31] (see Fig. 5a); however the net pairing symmetry of the order parameter remains a chiral *p*-wave at the interface region, with a slightly reduced magnitude. As the interface transparency is lowered, the p_x component of the order parameter will be strongly suppressed, while the p_y slightly enhanced[31,32] (Fig. 5b). Considering our data at the first cool down the transparency is high; if the induced order parameter is of the type *p*+*s* it will preserve the same symmetry at the interface. In this case, a Fraunhofer-like magnetic pattern is expected[23], as we have found in our experiment. After thermal cycling, however, the critical current is suppressed by orders of magnitude (Fig. 2). This fact cannot solely be attributed to a change in interface transparency due to plastic deformations induced by compressive strain (buckling). The strong suppression of I_C is, on the other hand, fully consistent with a change in pairing symmetry of the *p*+*s* OP. In particular, as theoretically predicted[31,32] the chiral *p*-wave term will assume a predominantly p_y-wave form at the interfaces (with the p_y lobe parallel to the interface).

If one considers only the chiral term of the *p*+*s* OP its amplitude and phase at the S'IN interface are shown in Figures 5c and 5d for a highly and low transparent interface

respectively[32]. The chiral p term, of the total OP, is mainly transformed in p_y for low transparency barriers. Theory shows that in p_y-p_y junctions the critical current becomes strongly suppressed even for a slight increase of scattering in the junction[33]. This is therefore fully consistent with the observed reduction, of orders of magnitude in I_C, after thermal cycling. Secondly, such a change in pairing symmetry also explains the inversion of the Fraunhofer pattern with a dip at $B = 0$ when the S'IN interface transparency is lowered. For a predominantly p_y-wave OP at the interface, the occurrence of scattering in the normal region of the junction will couple quasiparticle trajectories, emerging from positive p_y lobe of the OP on one side of the junction, with trajectories that probe the negative p_y lobe on the other side of the junction. This corresponds to a net π-phase shift in the Josephson coupling (see Fig. 6a and 6b). Here it is worth pointing out that while the buckling wave in the nanogap area can partially be responsible for the reduction of the Josephson current (and possibly for a non homogenous distribution of J_C across the width of the junction) it cannot account for the peculiar dip of the Fraunhofer patter at B=0, requiring a net π-phase shift between the electrodes. While the above scenario provides a possible route for introducing 0- and π-trajectories in the system, we underline that an s-wave component of the OP simultaneously exists. We speculate that for π-shifted trajectories to become possible, it might be of importance that the p_y-wave component is enhanced compared to the s-wave one since the p- and s-wave condensates are not separated due to the spin-mixing resulting from the normal-state TI dispersion with spin momentum locking.

In films with pronounced pyramidal nano-domains, like the flakes used in our experiment, the edges have proven to host an enhanced density of states[34,35] and to be preferential trajectories[36]. Aharonov-Bohm oscillations in the magneto-resistance of thin films, where

orbits around the triangle edges define the loop areas[36] have been recently detected, demonstrating that the triangle's corners and more in general step-edges work as scattering centers. To show that this effect is also observed in our Bi_2Te_3 flakes we have measured the magneto-transport down to 20 mK temperatures. We observe clear periodic magneto-resistance oscillations, arising from coherent scattering of electron waves from the corners of the pyramidal domains and/or from the points where two domains merge, with a period corresponding to the morphology of the flake (see Supplementary Note 4). In this scenario, among the quasiparticles crossing the Bi_2Te_3 normal channel, the ones undergoing large scattering angles at the corners or step-edges of the pyramidal nano-domain, will probe a phase shift of π on the other side of the junction. The quasi-particles trajectories, instead, that do not undergo scattering events in the normal channel (e.g. coupling lobes of the same sign with each other) give a conventional 0 coupling. The schematics of the scattering processes are shown in Fig. 6b. The net result is that the total supercurrent is partially cancelled by these competing contributions, which amounts to a suppressed I_C at zero field.

This simple explanation has also a direct microscopic analog in terms of Andreev levels mediated transport in a Josephson junction[37]. Indeed a peculiarity of our measurement is the transition of the magnetic pattern to a conventional Fraunhofer type, for temperatures around 100 mK when the dip at zero field flattens out (Fig. 4b). This crossover has been theoretically predicted in the framework of low transparent Josephson junctions involving d-wave HTS[37,38]. The physics behind this phenomenology is connected to the presence of zero energy Andreev bound states, or Mid Gap States (MGS), characteristic of Josephson junctions with an OP with a nontrivial internal phase[37]. For the case of Figure 5b, the p_x component, responsible of the MGS formation[31], is non zero on distances where Andreev

reflection takes place[37] (which are given by the coherence length in S'). Midgap states are therefore formed on both sides of the junction and their resonant coupling gives an additional Josephson transport channel proportional to $D^{0.5}$ (instead of D as for conventional Andreev level mediated transport). When the MGS carrying current dominates at very low temperature[37,38] and scattering events take place at triangle corners, the equilibrium phase difference of the system is at π, corresponding to a negative current. For straight quasiparticle trajectories the MGS current gives a conventional 0 phase character ground state.

Formally, this scenario is similar to artificially designed 0-π ferromagnetic Josephson junctions where multiple connected segments are π-shifted compared to each other[39]. In this case, a similar inverted pattern is observed. The dip of the Josephson current at $B = 0$ is thus the proof of a superconducting order parameter with an internal phase-structure, which can cause either 0 or π couplings, precisely as seen in our setup (see Supplementary Note 5).

In a generic junction, the contribution to the current is due to both the resonant MGS and the conventional Andreev bound states. At larger temperature the contributions of MGSs current cancels out since both MGSs carrying forward and backwards current are populated[37] and therefore the conventional Andreev levels current will dominate. This leads to a peculiar π to 0 transition by increasing the temperature. Signatures of such a crossover have been reported in a Superconducting Quantum Interference Device (SQUID) geometry for *d*-wave junctions[40]. However those results were never confirmed, posing serious doubts on the effective possibility to detect a π-0 transition from the temperature dependence of the

magnetic patterns. Our experiment is therefore one of the first demonstrations of Josephson transport mediated by MGS.

Clearly the dip at B=0 in the magnetic pattern is also compatible with a $d_{x^2-y^2}$ wave order parameter[41]. We can rule out this possibility since the $d_{x^2-y^2}$ OP does not change symmetry depending on the interface transparency[37] and therefore cannot account for the dramatic modifications of the magnetic field response of the junctions upon thermal cycling. An helical p_x+p_y OP can instead be compatible with our entire experimental scenario. However this OP symmetry does not come directly from the theoretical works[1,14,41] so the possibility to induce an helical p_x+p_y OP needs further theoretical assessment.

To further check the conjecture that step-edges and pyramidal corners act as scattering centers, we have fitted the temperature dependence of the critical current $I_C(T)$ of the high transparency junctions. We consider that our S'INIS' junction is characterized by insulating barriers with transparencies D_1 and D_2, which are separated by a distance L [42]. The disorder in the normal channel is characterized by a mean free path l_e. As previously discussed, in case of high transparency barriers the junction behaves similarly to conventional s-wave junctions[43]; in this case we do not lose generality by modeling the S' superconductor with an s-wave OP. The Josephson current for an S'INIS' junction in the clean limit $l_e \gg L$ has been derived in a previous work[8]. To fit our data, we have modified the original result of Ref. [8] in two ways (see Supplementary Note 6): (i) by adapting it to the two dimensional Dirac character of the surface states, and (ii) by extending it into the regime $l_e \approx L$ which is achieved by changing the flight time expression of the electrons between the leads. We have verified that our approach well reproduces the Eilenberger theory for purely

ballistic junctions and the Usadel theory for short diffusive junctions. Figure 7 shows the $I_C(T)$ of the junction of Fig. 1c. The solid curve is the fit by considering the geometrical dimensions and $l_e = 130$ nm. The extracted value for the mean free path clearly supports our assumption that few scattering centers are present in the barrier and that some quasiparticles while crossing the TI channel will undergo a single scattering event. The value of the normal state resistance extracted from the fit is higher than the experimental one, which can be explained by shunting effect of the bulk of the Bi_2Te_3 [8] (see Supplementary Note 6).

It is worth mentioning that we did not observe any apparent correlation between the orientation of the nano-pyramidal domains and that of the electrodes. This is not surprising; the basic mechanism to get an inverted magnetic field pattern, is the occurrence of 0 and π trajectories within the nanogap and they can be obtained for whatever orientation of the triangles with respect of the electrode, provided that some of the corners and/or the points where two domains merge fall within the Bi_2Te_3 nanogap (see Supplementary Note 4).

Finally we would like to point out that magneto transport measurements (Supplementary Note 4) have clearly shown that scattering mechanisms, connected to the morphology of the Bi_2Te_3 flakes, take place in the junction channel, which is instrumental to get π trajectories. However the interpretation of our measurements does not change if other scattering mechanisms are also involved.

To conclude it is worth discussing if the interpretation we have provided of our experiment would change if we would also consider a parallel Josephson contribution due to the transport through the bulk with an *s*-wave OP. Cooper pair transport through the bulk

would just act as 0 trajectories effectively lifting the value of the Josephson current at zero external magnetic field, however leaving unaltered the dip structure at zero field of the magnetic pattern.

Methods:

Materials and device fabrication

Bi_2Te_3 thin films have been deposited by molecular beam epitaxy on a GaAs (100) substrate with a 2° vicinal cut. Prior to the growth, a one minute Te soaking to the GaAs surface was carried out for passivation purpose. Then, the growth started at a temperature of 180 °C, when both Te and Bi sources were opened, and ended at a thickness of 80 nm after one hour. The films have been grown with a high Te/Bi flux ratio, to obtain high quality crystallinity, as verified by X-Ray Diffraction (XRD) analysis[44].

The films show characteristic aligned pyramidal domains (see Fig. 1b). This morphology is different with respect to the growth on exact substrates, where two types of pyramidal domains rotated by 60° with respect to each other are observed[20]. As verified by XRD analysis, our films show 86% single domain, which indicates that the vicinal cut in the substrate leads to suppression of twin boundaries, as also reported in literature[20]. The transport properties have been characterized by magneto-transport measurements; the films show an effective surface carrier density of 4×10^{13} cm^{-2} and mobility above 2000 $cm^2V^{-1}s^{-1}$ (at the temperature of T = 2 K).

Josephson junctions using Al electrodes have been realized by transferring the flakes on a Si/SiO_2 substrate. To improve the adhesion with the Al electrodes a thin layer (3 nm) of Pt is

deposited in situ on the surface of the flake, previously cleaned by a short (10 s) Ar^+ ion milling[45,46].

Data availability

All relevant data are available from the authors.

References:

1 Fu, L. & Kane, C. L. Superconducting proximity effect and majorana fermions at the surface of a topological insulator. *Phys. Rev. Lett.* **100**, 096407, doi:10.1103/PhysRevLett.100.096407 (2008).

2 Beenakker, C. W. J. Search for Majorana Fermions in Superconductors. *Annu. Rev. Condens. Matter Phys.* **4**, 113-136, doi:10.1146/annurev-conmatphys-030212-184337 (2013).

3 Alicea, J. New directions in the pursuit of Majorana fermions in solid state systems. *Rep. Prog. Phys.* **75**, 076501, doi:10.1088/0034-4885/75/7/076501 (2012).

4 Qi, X. L., Hughes, T. L., Raghu, S. & Zhang, S. C. Time-reversal-invariant topological superconductors and superfluids in two and three dimensions. *Phys. Rev. Lett.* **102**, 187001, doi:10.1103/PhysRevLett.102.187001 (2009).

5 Hasan, M. Z. & Kane, C. L. Colloquium: Topological insulators. *Rev. Mod. Phys.* **82**, 3045-3067, doi:10.1103/RevModPhys.82.3045 (2010).

6 Qi, X.-L., Witten, E. & Zhang, S.-C. Axion topological field theory of topological superconductors. *Phys. Rev. B* **87**, doi:10.1103/PhysRevB.87.134519 (2013).

7 Sacepe, B. *et al.* Gate-tuned normal and superconducting transport at the surface of a topological insulator. *Nat. Commun.* **2**, 575, doi:10.1038/ncomms1586 (2011).

8 Veldhorst, M. *et al.* Josephson supercurrent through a topological insulator surface state. *Nat. Mater.* **11**, 417-421, doi:10.1038/nmat3255 (2012).

9 Oostinga, J. B. *et al.* Josephson Supercurrent through the Topological Surface States of Strained Bulk HgTe. *Phys. Rev. X* **3**, 021007, doi:10.1103/PhysRevX.3.021007 (2013).

10 Galletti, L. *et al.* Influence of topological edge states on the properties of Al/Bi2Se3/Al hybrid Josephson devices. *Phys. Rev. B* **89**, 134512, doi:10.1103/PhysRevB.89.134512 (2014).

11 Kurter, C., Finck, A. D., Hor, Y. S. & Van Harlingen, D. J. Evidence for an anomalous current-phase relation in topological insulator Josephson junctions. *Nat. Commun.* **6**, 7130, doi:10.1038/ncomms8130 (2015).

12 Hart, S. *et al.* Induced superconductivity in the quantum spin Hall edge. *Nat. Phys.* **10**, 638-643, doi:10.1038/Nphys3036 (2014).

13 Pribiag, V. S. *et al.* Edge-mode superconductivity in a two-dimensional topological insulator. *Nat. Nanotechnol.* **10**, 593-597, doi:10.1038/nnano.2015.86 (2015).

14 Tkachov, G. & Hankiewicz, E. M. Helical Andreev bound states and superconducting Klein tunneling in topological insulator Josephson junctions. *Phys. Rev. B* **88**, doi:10.1103/PhysRevB.88.075401 (2013).

15 Kallin, C. Chiral p-wave order in Sr2RuO4. *Rep. Prog. Phys.* **75**, 042501, doi:10.1088/0034-4885/75/4/042501 (2012).

16 Cho, S. *et al.* Symmetry protected Josephson supercurrents in three-dimensional topological insulators. *Nat. Commun.* **4**, 1689, doi:10.1038/ncomms2701 (2013).

17 Sochnikov, I. *et al.* Nonsinusoidal current-phase relationship in Josephson junctions from the 3D topological insulator HgTe. *Phys. Rev. Lett.* **114**, 066801, doi:10.1103/PhysRevLett.114.066801 (2015).

18 Van Harlingen, D. J. Phase-sensitive tests of the symmetry of the pairing state in the high-temperature superconductors—Evidence for d_{x2-y2} symmetry. *Rev. Mod. Phys*. **67**, 515-535, doi:10.1103/RevModPhys.67.515 (1995).

19 Tsuei, C. C. & Kirtley, J. R. Pairing symmetry in cuprate superconductors. *Rev. Mod. Phys*. **72**, 969-1016, doi: 10.1103/RevModPhys.72.969 (2000).

20 Tarakina, N. V. *et al.* Suppressing Twin Formation in Bi_2Se_3 Thin Films. *Adv. Materi. Interf.* **1**, 1400134, doi:10.1002/admi.201400134 (2014).

21 Flensberg, K., Hansen, J. B. & Octavio, M. Subharmonic energy-gap structure in superconducting weak links. *Phys. Rev. B* **38**, 8707-8711, doi:10.1103/PhysRevB.38.8707 (1988).

22 Abay, S. *et al.* Charge transport in InAs nanowire Josephson junctions. *Phys. Rev. B* **89**, doi:10.1103/PhysRevB.89.214508 (2014).

23 Potter, A. C., & Fu, L. Anomalous supercurrent from Majorana states in topological insulator Josephson junctions. *Phys. Rev. B* **88**, 121109(R), doi:10.1103/PhysRevB.88.121109 (2013).

24 Molenaar, C. G., Leusink, D. P., Wang, X. L. & Brinkman, A. Geometric dependence of Nb-Bi_2Te_3-Nb topological Josephson junction transport parameters. *Supercond. Sci. Technol.* **27**, 104003, doi:10.1088/0953-2048/27/10/104003 (2014).

25 Williams, J. R. *et al.* Unconventional Josephson effect in hybrid superconductor-topological insulator devices. *Phys. Rev. Lett.* **109**, 056803, doi:10.1103/PhysRevLett.109.056803 (2012).

26 Liu, W. *et al.* Anisotropic interactions and strain-induced topological phase transition in Sb_2Se_3 and Bi_2Se_3. *Phys. Rev. B* **84**, 245105, doi:https://doi.org/10.1103/PhysRevB.84.245105 (2011).

27 Young, S. M. *et al.* Theoretical investigation of the evolution of the topological phase of Bi_2Se_3 under mechanical strain. *Phys. Rev. B* **84**, 085106, doi:10.1103/PhysRevB.84.085106 (2011).

28 Zeljkovic, I. *et al.* Strain engineering Dirac surface states in heteroepitaxial topological crystalline insulator thin films. *Nat. Nanotechnol.* **10**, 849-853, doi:10.1038/nnano.2015.177 (2015).

29 Liu, Y. *et al.* Tuning Dirac states by strain in the topological insulator Bi_2Se_3. *Nat. Phys.* **10**, 294-299, doi:10.1038/nphys2898 (2014).

30 Bowden, N., Brittain, S., Evans, A. G., Hutchinson, J. W., & Whitesides, G. M. Spontaneous formation of ordered structures in thin films of metals supported on an elastomeric polymer. *Nature* **393**, 146-149, doi:10.1038/30193 (1998).

31 Tanuma, Y., Tanaka, Y. & Kashiwaya, S. Theory of the proximity effect at the interface of a normal metal and triplet p-wave superconductor in the clean limit. *Phys. Rev. B* **74**, 024506, doi:10.1103/PhysRevB.74.024506 (2006).

32 Matsumoto, M. & Sigrist, M. Quasiparticle States near the Surface and the Domain Wall in apx±ipy-Wave Superconductor. *J. Phys. Soc. Jpn.* **68**, 994-1007, doi:10.1143/jpsj.68.994 (1999).

33 Asano, Y., Tanaka, Y., Yokoyama, T. & Kashiwaya, S. Josephson current through superconductor/diffusive-normal-metal/superconductor junctions: Interference

effects governed by pairing symmetry. *Phys. Rev. B* **74**, 064507, doi:10.1103/PhysRevB.74.064507 (2006).

34 Alpichshev, Z., Analytis, J. G., Chu, J. H., Fisher, I. R., & Kapitulnik, A. STM imaging of a bound state along a step on the surface of the topological insulator Bi_2Te_3. *Phys. Rev. B* **84**, 041104, doi:10.1103/PhysRevB.84.041104 (2011).

35 Liu, Y., Weinert, M., & Li, L. Spiral growth without dislocations: molecular beam epitaxy of the topological insulator Bi_2Se_3 on epitaxial graphene/SiC (0001). *Phys. Rev. Lett.* **108**, 115501, doi:10.1103/PhysRevLett.108.115501 (2012).

36 Kandala, A., Richardella, A., Zhang, D., Flanagan, T. C. & Samarth, N. Surface-sensitive two-dimensional magneto-fingerprint in mesoscopic Bi2Se3 channels. *Nano Lett.* **13**, 2471-2476, doi:10.1021/nl4012358 (2013).

37 Lofwander, T., Shumeiko, V. S. & Wendin, G. Andreev bound states in high-T-c superconducting junctions. *Supercond. Sci. Technol.* **14**, R53-R77, doi:10.1088/0953-2048/14/5/201 (2001).

38 Tanaka, Y. & Kashiwaya, S. Theory of Josephson effects in anisotropic superconductors. *Phys. Rev. B* **56**, 892-912, doi:10.1103/PhysRevB.56.892 (1997).

39 Weides, M. *et al.* 0-pi Josephson tunnel junctions with ferromagnetic barrier. *Phys. Rev. Lett*. **97**, 247001, doi:10.1103/PhysRevLett.97.247001 (2006).

40 Testa, G. *et al.* Midgap state-based π-junctions for digital applications. *Appl. Phys. Lett.* **85**, 1202, doi:10.1063/1.1781744 (2004).

41 Black-Schaffer, A. M. & Balatsky, A. V. Proximity-induced unconventional superconductivity in topological insulators. *Phys. Rev. B* **87**, doi:10.1103/PhysRevB.87.220506 (2013).

42 Galaktionov, A. V. & Zaikin, A. D. Quantum interference and supercurrent in multiple-barrier proximity structures. *Phys. Rev. B* **65**, 184507, doi:10.1103/PhysRevB.65.184507 (2002)

43 Sawa, Y., Yokoyama, T., Tanaka, Y. & Golubov, A. A. Quasiclassical Green's function theory of the Josephson effect in chiral p-wave superconductor/diffusive normal metal/chiral p-wave superconductor junctions. *Phys. Rev. B* **75**, 134508, doi:10.1103/PhysRevB.75.134508 (2007).

44 Fülöp, A. *et al.* Phase transition of bismuth telluride thin films grown by MBE. *Appl. Phys. Express* 7(4), 045503, doi: 10.7567/APEX.7.045503 (2014).

45 Galletti, L. *et al.* Josephson effect in Al/Bi 2 Se 3/Al coplanar hybrid devices. *Phyica C* 503, 162-165, doi: 10.1016/j.physc.2014.04.047 (2014).

46 Andzane, J. *et al.* Catalyst-free vapour–solid technique for deposition of Bi2Te3 and Bi2Se3 nanowires/nanobelts with topological insulator properties. *Nanoscale* 7(38), 15935-15944, doi: 10.1039/C5NR04574F (2015).

Acknowledgments:

The work has been supported by the Swedish Foundation for Strategic Research (SSF) under the project "Graphene based high-frequency electronics" and by the Knut and Alice Wallenberg Foundation under the project "Dirac Materials." The authors would also like to thank J. Kirtley, A. Leggett, S. Kubatkin, P. Lucignano, A. Tagliacozzo, M. Fogelström, M. Eschrig, P. Burset, V. Shumeiko and A. Black-Shaffer for inspiring discussions. This work was partly supported by the Research Council of Norway through its Centres of Excellence funding scheme, project number 262633, QuSpin.

Author contributions:

S.C. and L.G. have fabricated the samples and performed the measurements. S.W. and Y.S have grown the Bi2Te3 thin films. D.G. and J.L. have contributed with theoretical insights and F.T. with discussions. G.K., E.O., A.K., R.A., R.B. have performed morphological and structural characterizations of the devices. F.L. and T.B. have interpreted the measurements in collaboration with all authors. F.L has written the paper with inputs from all co-workers.

Additional information:

Supplementary Information accompanies this paper.

Competing interests The authors declare no competing financial interests

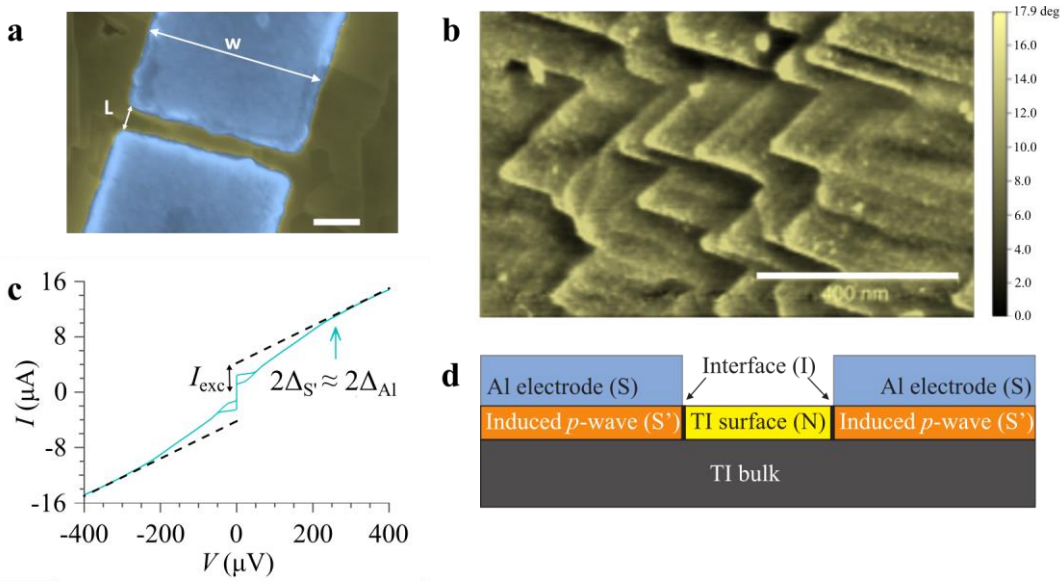

Fig. 1 Morphological and transport characterization of a typical proximity based Bi_2Te_3 Josephson junction. (a) Scanning Electron Microscope image of a junction made using an exfoliated flake. The light blue areas define the Al/Pt electrodes while the Bi_2Te_3 flake is shown in yellow. Scale bar: 200 nm. **(b)** Atomic Force Microscope image of a Bi_2Te_3 thin film grown on GaAs substrate showing a typical growth with aligned pyramidal domains. Scale bar: 400 nm. **(c)** IVC of a typical junction ($w = 1$ μm, $L = 200$ nm) measured at 20 mK (cyan). The resistive branch shows a neat change of slope at a voltage $V \approx 260$ μV (cyan arrow) that corresponds to approximately $2\Delta_{Al}$ for the thickness of the electrodes[22]. The black arrow indicates the value of the extracted excess current. **(d)** Cross section schematics of the effective device under consideration. The transport properties can be assimilated to those of a S'INIS' Josephson junction where S' represents the induced superconductor in the Bi_2Te_3.

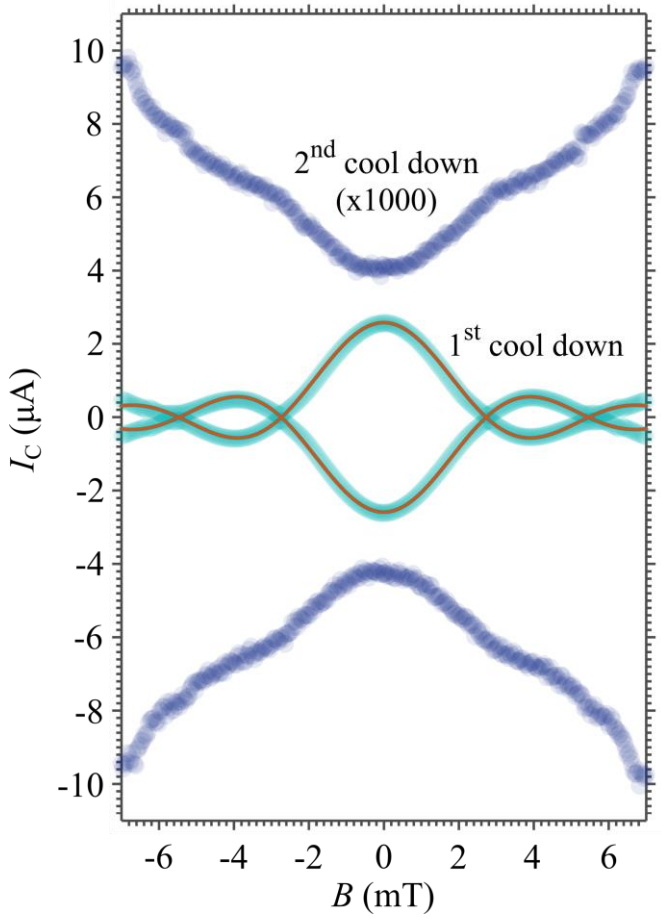

Fig. 2 Magnetic field pattern of a typical junction before and after the thermal cycle. Critical current I_C dependence on the externally applied magnetic field B for the junction of Fig. 1c at 20 mK, before (cyan) and after (blue) the thermal cycle. At the first cool down the $I_C(B)$ dependence shows a conventional Fraunhofer dependence fitted with the expression $I_C(B) = I_C(0)\left|{\sin(\pi\,\phi/\Phi_0)}/{(\pi\,\phi/\Phi_0)}\right|$ (red line) where $I_C(0)$ is the critical current at zero field, ϕ_0 is the flux quantum, and $\phi = BA_{\text{eff}}$ is the flux through the junction, being A_{eff} the effective area. After the thermal cycle (blue points), the critical current is dramatically reduced (the data points are multiplied by a factor 1000 for clarity), and a dip at $B = 0$ appears.

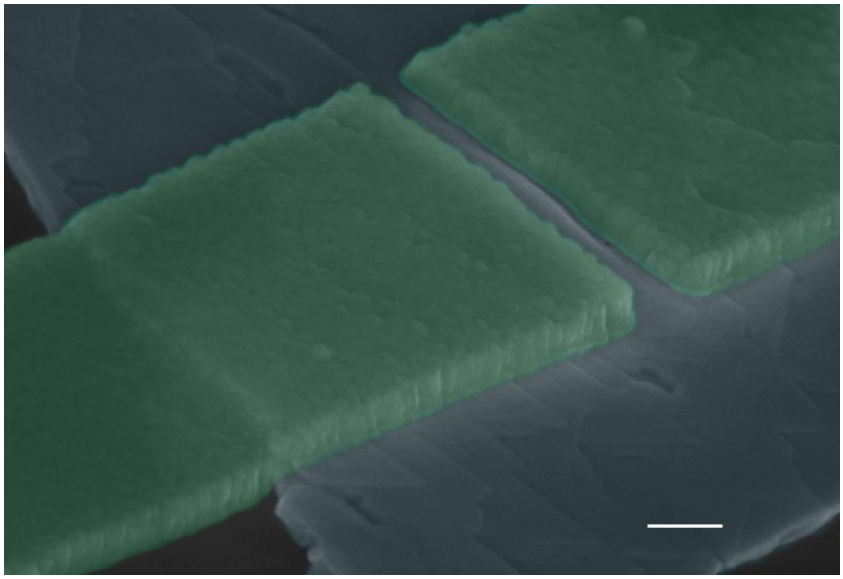

Fig. 3 Colored SEM image of a typical junction after the second cool down. The picture (scale bar: 200 nm) show a junction presenting an inverted Josephson magnetic pattern, after the second cool down. A clear buckling feature, induced by a compressive strain, is visible in the nanogap.

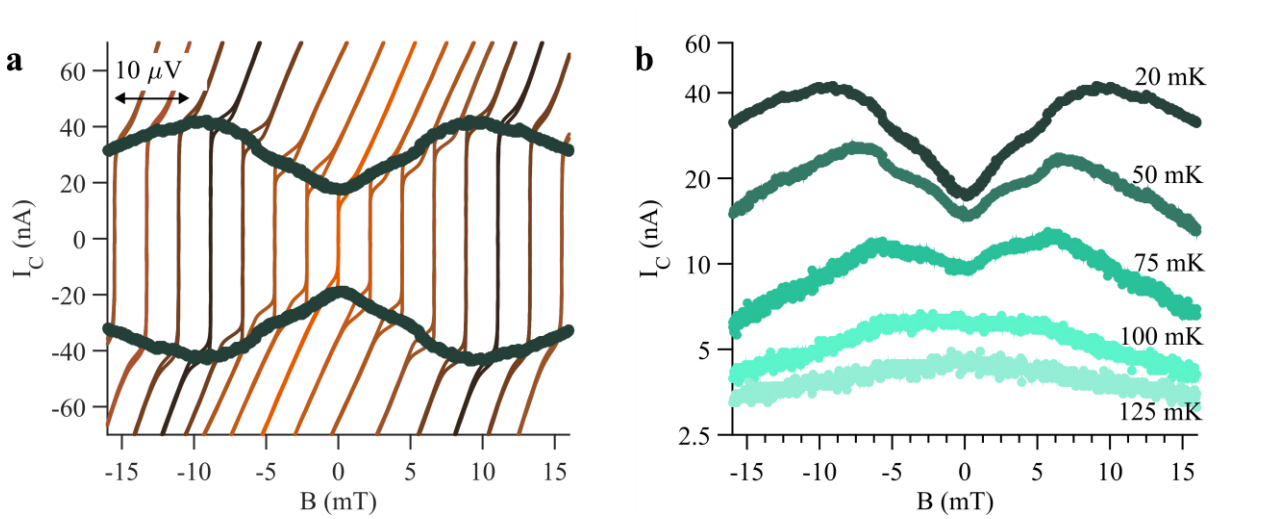

Fig. 4 Current voltage characteristics as a function of magnetic field and temperature for a typical junction after thermal cycling. (a) IVCs of a second device ($w = 500$ nm and $L = 100$ nm) are shown as a function of B after thermal cycling. The curves are shifted in voltage by a value proportional to the magnetic field. The green points represent the magnetic pattern of the junctions obtained using a voltage criterium $V = 600$ nV. Also in this case the magnetic pattern presents a very pronounced dip at $B = 0$. **(b)** Evolution of the magnetic pattern shown in panel (a) as a function of the temperature. The dip flattens out at a temperature close to 100 mK.

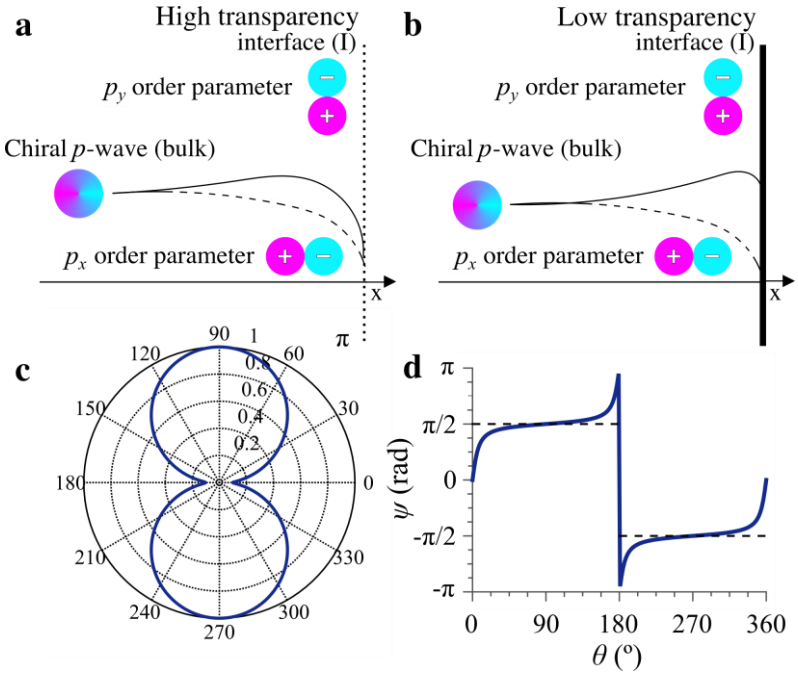

Fig. 5 Proximity induced OP on the surface of Bi_2Te_3. We consider only the chiral p_x+ip_y part of the total p+s OP. Close to the interface I the chiral term is modified: the p_x (dashed line) and p_y (straight line) components exhibit different magnitude. In case of high transparency interface **(a)** the two components are both suppressed in equal manner and the resulting interface OP still preserve the p_x + ip_y wave character. For a low transparency interface **(b)**, the p_x component is highly suppressed while the p_y slightly enhanced. The resulting OP has a predominantly p_y character. Panel **(c)** shows the amplitude of the resulting interface OP by considering a mixture p_y+iαp_x, with $\alpha = 0.1$. This corresponds to the reduction of p_x on distances of the order of the coherence length of S' [28]. The corresponding phase is shown in **(d)**.

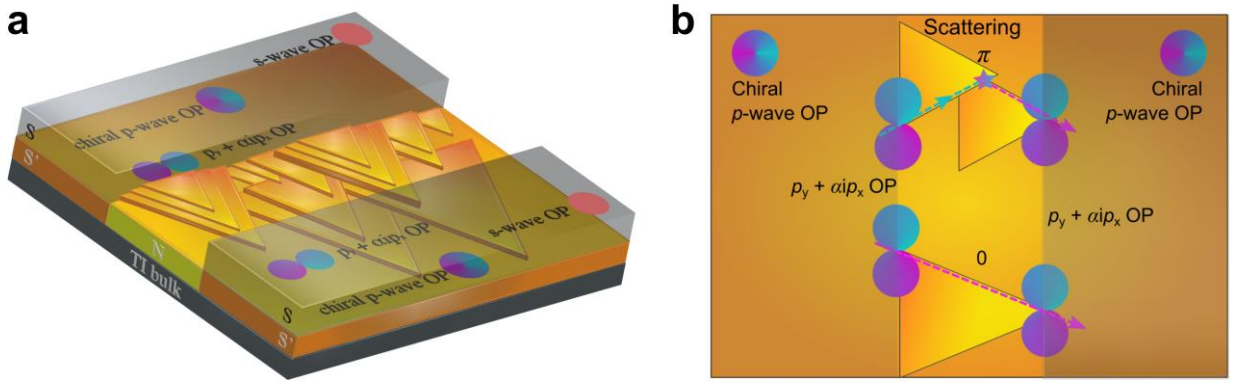

Fig. 6 Sketch of the device showing the induced order parameter and the occurrence of π-paths across the junction. (a) Three dimensional sketch of the Bi_2Te_3 device. The Al electrodes (S) induce an effective *p*+*s*-wave superconductivity on the surface of the TI. In the picture we consider only the chiral term of the total OP. In close proximity of a low transparency interface the chiral p_x+ip_y changes symmetry resulting in a predominant p_y component (see main text for details). **(b)** Top view of the device. The occurrence of scattering at the pyramid corners and/or at the merging points of two pyramidal domains, in the N region of the junction, makes quasiparticle trajectories emerging from a negative p_y lobe (blue arrow) on one side of the junction to couple with trajectories that probe the positive p_y lobe (red arrow) on the other side of the junction. In case of scattering-free transport in the N region the quasiparticles trajectories probe the same phase in both electrodes (red arrows).

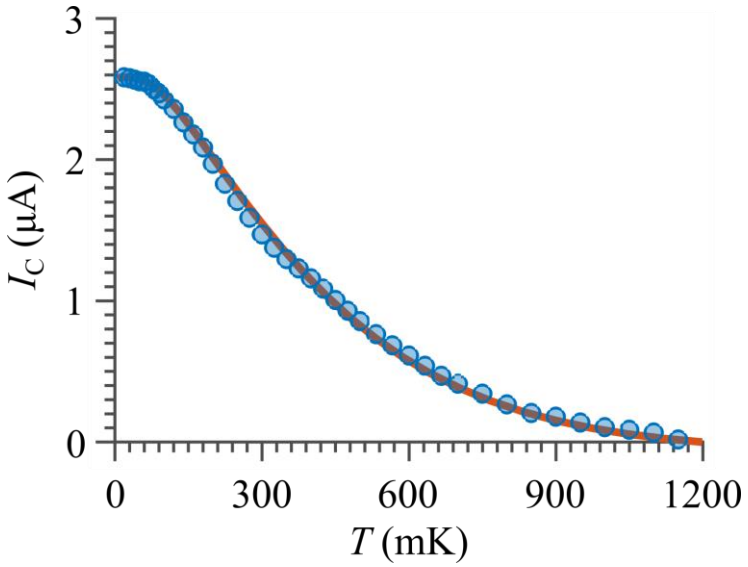

Fig. 7 Temperature dependence of the Josephson current for a high transparency junction. Critical current as a function of the temperature, measured at the first cool down for the junction of Fig. 1c (full circles). The red line is the fitting considering a quasi-ballistic transport model (see Supplementary Note 6 and Supplementary Equations (5-10)). We extract the following fitting parameters for the mean free path $l_e = 130$ nm and the transparencies of the two barriers $D_1 = D_2 = 0.98$. From Supplementary Equation (13) the expected normal state resistance is $R_N = 70$ Ω. The experimental value for R_N is instead 35 Ω. The discrepancy between these two values can be attributed to the shunting effect of the bulk of the Bi_2Te_3 flake.

Device	I_C^{before} μA	I_C^{after} μA	R_N^{before} Ω	R_N^{after} Ω	$I_C R_N^{before}$ μeV	$I_C R_N^{after}$ μeV	w μm	L nm	$\frac{I_C^{after}}{I_C^{before}}$	$\frac{R_N^{after}}{R_N^{before}}$
JM10	2.6	0.002	36	215	89	0.4	1	200	0.07%	6.0
JM5	-	0.017	-	216	-	3.6	0.5	100	-	-
JM11	1.8	0.085	41	62	47	5	1	300	4%	1.5
SF2	0.58	0	15	20	9	0	2	100	0%	1.3
JM1	0.6	-	86	-	54	-	0.5	200	-	-
SM4	9.3	0.060	17	61	144	8.6	1.5	100	0.6%	3.6
SD3	0.36	0.040	18	53	6	2	2	250	11%	2.9
SF3	2.2	0.030	10	25	22	0.7	2	100	1.4%	2.5
SF8	3.2	0.180	11	25	35	4.5	2	100	5.6%	2.3
SD4	0.6	0.02	32	52	2	1	2	250	3%	1.6
SF4	19.8	6.600	3.6	5.6	-	-	6	100	33%	1.5
SD2	0.52	0.012	17	20	9	0.2	4	250	2.3%	1.2
SD1	1.2	0.086	27	30	32	2.5	2	250	7.1%	1.1
SM1	11.0	-	15	-	151	-	1.5	100	-	-

Table 1: Relevant parameters for all the measured devices before and after the thermal cycle.
The critical current I_C, the normal resistance (measured above gap) R_N, the $I_C R_N$ product, the width of the device w (in case of a SQUID twice the junction) and the distance between the electrodes L are reported. Devices JM10, JM5, SM4, SF8 and SD1 showed inverted magnetic patterns in the second cool down. The devices JM10 and JM5 are those, whose data are shown in the text. The junctions start with a J in the device name, whereas the SQUIDs device names start with an S.

Supplementary Note 1. EFFECTIVE AREA OF A PLANAR JOSEPHSON JUNCTION

The effective area A_{eff} of a planar junction in the thin film limit $t < 2\lambda$, with t the film thickness and λ the London penetration depth, having a junction width, w, much smaller than the Pearl length, $\lambda_\perp = \lambda^2/t$, is well approximated by the following expression[1]

$$A_{\text{eff}} \approx wL + w^2/1.82 \; . \tag{1}$$

Here L is the distance between the electrodes (see Supplementary Figure 1). For junction widths larger than the Pearl length, Supplementary Equation (1) is not anymore valid and the effective area has to be computed numerically.

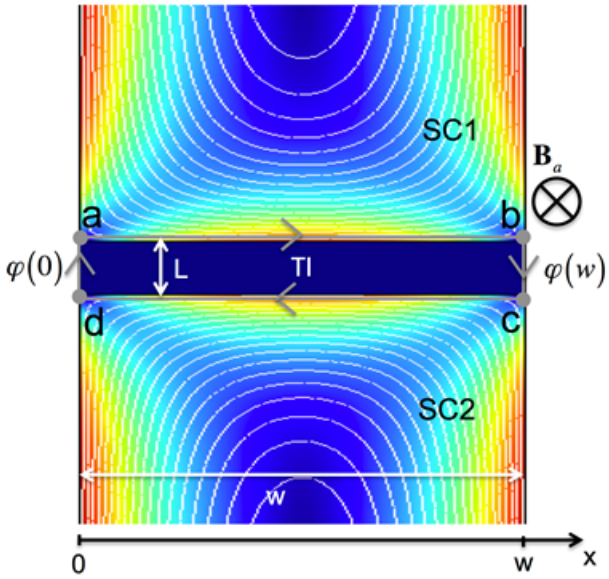

Supplementary Figure 1: **Supercurrent density distribution in a planar Josephson junction.** Sketch of two superconducting electrodes (SC1, SC2) contacted to a normal conducting channel (TI). The gray loop indicated the path integral used in Supplementary Equation (4). B_{a} is the externally applied magnetic field. The white lines indicate the current flow direction of the screening current and the color-coding in the electrodes reflects the amplitude of the screening current density (red: large, blue: small).

The effective area can be determined numerically as it follows.

First we calculate the Meissner screening currents in the superconducting electrodes by solving the Maxwell London equations on the junction geometry in the presence of an externally applied magnetic field:

$$\mu_0 \boldsymbol{\nabla} \times (\lambda^2 \cdot \mathbf{j}) + \mathbf{B} = 0 \; ; \qquad \boldsymbol{\nabla} \times \mathbf{B} = \mu_0 \mathbf{J} \; . \tag{2}$$

Here μ_0 is the vacuum permeability, $\mathbf{j}$ is the supercurrent density in the electrodes, and $\mathbf{B}$ is the magnetic induction containing the externally applied field, B_a, and the field generated by the supercurrents.

Next we need to calculate the difference between the gauge invariant phase differences across the junction at the left edge $\phi(0)$ and right edge $\phi(w)$ of the junction (see Supplementary Figure 1). From the above calculated Meissner currents and resulting magnetic fields we can readily compute $\Delta\phi = \phi(w) - \phi(0)$ making use of the property that the superconducting phase is single valued in the electrodes:

$$\Delta\phi = \frac{2\pi}{\phi_0}\oint \mathbf{A}\cdot\partial\mathbf{l} + \mu_0\lambda^2\left[\int_a^b \mathbf{j}\cdot\partial\mathbf{l} + \int_c^d \mathbf{j}\cdot\partial\mathbf{l}\right]. \tag{3}$$

Here $\phi_0 = 2\cdot 10^{-15}$ Vs is the superconducting flux quantum and $\mathbf{A}$ is the vector potential with $\mathbf{B} = \boldsymbol{\nabla}\times\mathbf{A}$. The closed path integral in the first term of the right hand side of the equation is taken along a loop enclosing the two edges of the junction at $x = 0$ and $x = w$. For the loop indicated in Supplementary Figure 1 the closed path integral corresponds to the total magnetic flux through the normal conductor in the junction. The line integrals in the second term of the right hand side of the Supplementary Equation (3) are taken only within the superconducting electrodes, i.e. from point a to b in the upper electrode, SC1, and from point c to d in the lower electrode, SC2 (see Supplementary Figure 1).

The effective area of the junction is finally obtained using the following standard expression:

$$A_\mathrm{eff} = \frac{\phi_0}{2\pi}\frac{\phi(w)-\phi(0)}{B_\mathrm{a}}. \tag{4}$$

In the above equation we assume a 2π periodic current phase relation along the junction.

For typical values of the London penetration depth ($\lambda \approx 100$ nm) for our 90 nm thick Al films[2], we obtain effective areas in the range $0.68-0.70\ \mu\mathrm{m}^2$, which is very close to the experimental value of $0.75\,\mu\mathrm{m}^2$. This strongly supports that a 2π periodic current phase relation mainly dominates the magnetic pattern of the critical current in our junctions.

Supplementary Note 2. EFFECTS OF THERMAL CYCLING AND OCCURRENCE OF $0-\pi$ TRANSITIONS IN THE MAGNETIC PATTERN

We have measured a total of 14 devices, including Josephson junctions and dc SQUIDs (see Table 1 in the main text), all fabricated with flakes from the same Bi_2Te_3 film. 12 devices have been measured in a second cool down; 5 of them showed unconventional magnetic patterns, with a minimum at zero field.

Supplementary Figure 2 shows another example of a high field inverted pattern for a dc SQUID (SF8). In this case there are two different modulations of the critical current: one is determined by the SQUID loop and the other is determined by the magnetic response of the single junctions forming the SQUID, which gives a dip at zero magnetic field in the convolution of the maxima of the SQUID modulation (Supplementary Figure 2A). Supplementary Figure 2B shows the magnetic pattern of the SQUID at low fields.

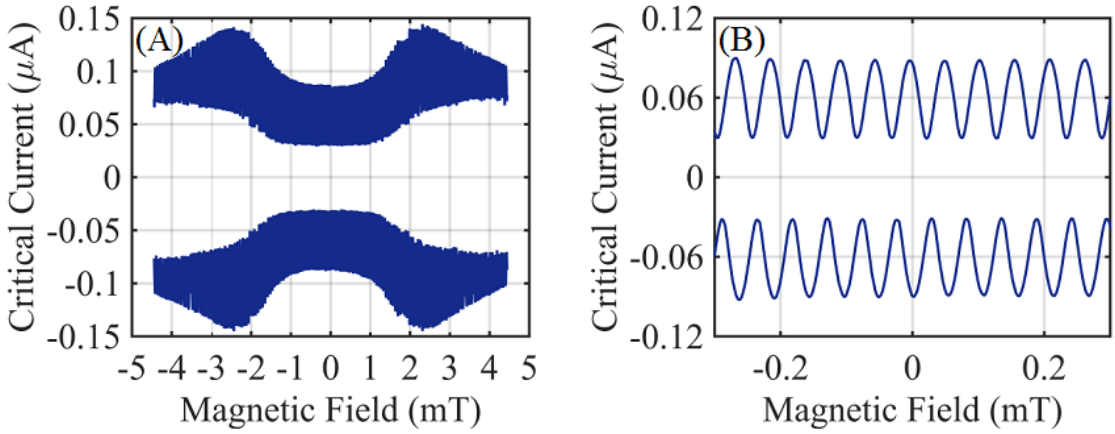

Supplementary Figure 2: **Critical current dependence as a function of the externally applied magnetic field of the SQUID FS8 at $T = 20$ mK.** Panel (**A**) clearly shows the feature of the magnetic response of the single junctions forming the SQUID, while the modulation due to the SQUID loop cannot be resolved on this scale (see text for details). The SQUID modulation becomes visible at low external magnetic fields (panel (**B**)).

Supplementary Note 3. MICROSCOPIC ORIGIN OF THE THERMAL CYCLING EFFECT

The thermal cycling effect has its origin in the role played by strain to tune the topological phase in TIs. In our devices, the complex interplay between the thermal properties of the substrate and the flake, the specifics of the interface between the Pt sticking layer and the Al, and the nanoscale dimensions of the devices have a fundamental role in creating plastic deformation at the TI nanogap separating the superconducting electrodes. The irreversible consequences of a compressive strain, induced by thermal cycling, manifest as peculiar buckling waves at the nanogap and a dramatic reduction of the Josephson current.

First principle calculations[3,4] have demonstrated that an in-plane tensile strain (pulling) leads to a out of plane compression where the quintuple layers are getting closer. An in plane compressive

strain (pushing) causes instead an out of plane expansion where the distance between quintuple layers is enhanced. The interquintuple interaction plays a dominant role in determining the topological phase: the consequence of an out of plane compression is a shift of the Dirac point closer to the valence band while an out of plane expansion leads to a gap opening at the Dirac point[3]. This argument is also used to explain why for example Sb_2Se_3 (with a larger c/a ratio compared to Bi_2Se_3) that is expected to be a TI in many ways, is instead a trivial insulator. It also tells that, in principle, strain can provide a tuning of the surface states of a topological insulator.

Strain is usually generated during the epitaxial growth of the material on the substrate, with lattice parameters different from those of the topological insulator. Recent reports have shown the tunability of the Dirac point with strain in thin topological crystalline insulator SnTe[5] and at grain boundaries in Sb_2Se_3 thin films[6].

Our experiment is quite different since our devices employ Bi_2Te_3 flakes exfoliated and transferred to a SiO_2/Si substrate, so a possible strain-related phenomenology cannot be attributed to the growth process.

The physics behind the peculiar transport properties of our devices is instead related to the enormous difference in the thermal expansion coefficient α of Bi_2Te_3 ($\approx 13.4 \times 10^{-6}$ °C^{-1}) and that of the SiO_2/Si substrate (0.5×10^{-6} °C^{-1}/2.4×10^{-6} °C^{-1}) where the flake is transferred. In our device configuration the Bi_2Te_3 is not grown on a SiO_2/Si substrate: the flake therefore will experience the huge difference in the thermal expansion coefficient only by the clamping to the substrate, which occurs through the patterning of the Al electrodes forming a nanometer sized gap junction.

At the first cool down, from room temperature to mK, the flake is prone to contract. However the Al electrodes will anchor the flake to the substrate making it experiencing the much smaller thermal coefficient of the SiO_2/Si. This leads to a tensile strain (pulling of the flake) which strongly concentrated in the part of the flake located at the nanogap. This important fact is related to the thermal expansion coefficient of Al ($\approx 23 \times 10^{-6}$ °C^{-1}) not much different from that of the Bi_2Te_3. For a good bonding between the Al and the flake, as the one provided by the Pt sticking layer, one can consider the Al electrodes and the flake under them as forming a quite homogenous material with a thickness more than twice that of the flake (the thickness of Al is roughly twice that of the flake). In this way most of the strain, provided by the Al electrodes and locking the flake to the substrate, is located at the thin Bi_2Te_3 nanogap, with a smaller thickness compared to that of the composite material Al/flake.

Since the tensile strain concentrates in the nanogap region, in this part of the flake the Dirac

node is shifted towards the valence band which makes the Bi_2Te_3 channel effectively more doped.

During the warming up of the sample the Bi_2Te_3 at the nanogap undergoes instead a compressive strain which opens a gap at the Dirac point. This compressive strain induces plastic deformation (the sample properties are completely changed after thermal cycling) and, if it overcomes a critical strain, can lead to a buckling of the Bi_2Te_3 channel forming the nanogap.

Supplementary Figure 3a shows a SEM top picture of one of the sample discussed in our paper. This specific picture does not show, very clearly, possible anomalous features of the flake inside

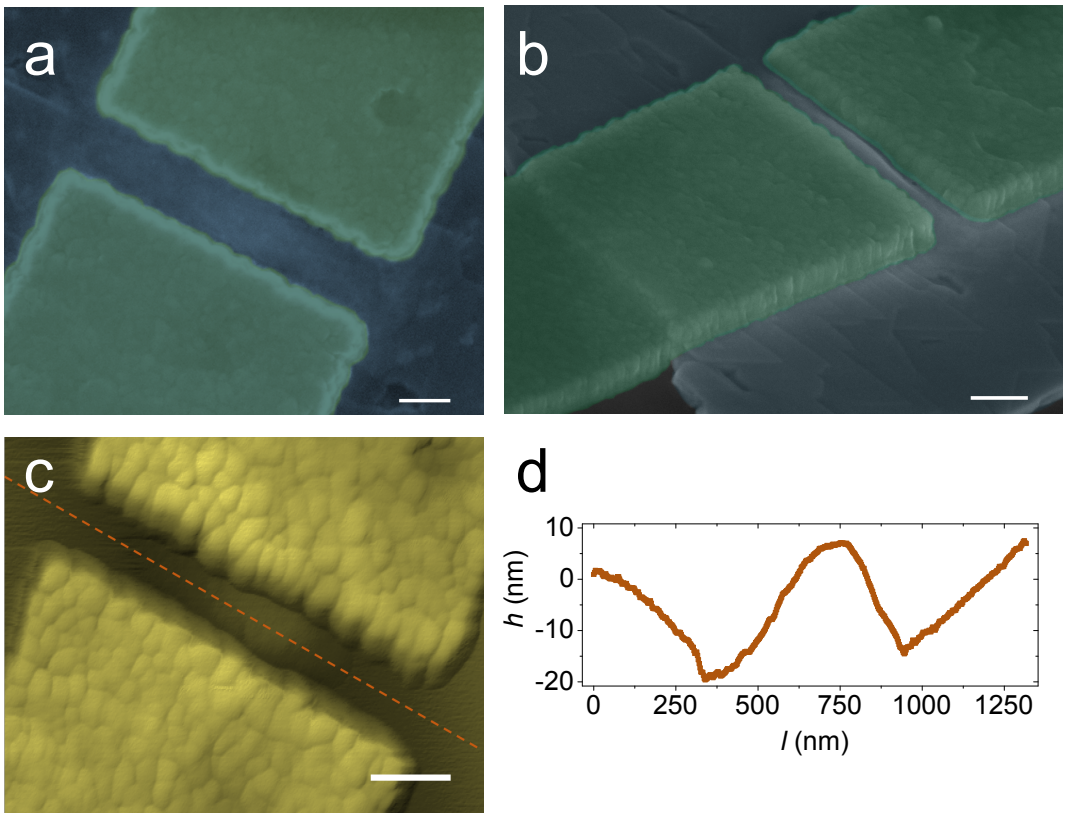

Supplementary Figure 3: **Colored SEM and AFM images for a junction showing a 0-π magnetic pattern.** This device is one of those discussed in our main manuscript (Pt interlayer). (**a**) SEM top view (scale bar: 200 nm); (**b**) tilted view (scale bar: 200 nm), green color represents the electrodes; (**c**) AFM height image (scale bar: 150 nm); (**d**) height profile along the junction.

the nanogap, except a region with a slightly brighter color. However by taking a SEM picture at an angle, shown in Supplementary Figure 3b, the brightness at the nanogap clearly manifests as a buckling feature[7]. To further evaluate the characteristics of such a buckling, we have performed AFM analysis to resolve the shape of the deformation inside the nanogap. Supplementary Figure 3c shows an AFM picture of the same junction, while Supplementary Figure 3d a line scan (orange

dashed line) taken inside the nanogap. The line scan has a very clear sinusoidal-like shape, a distinctive feature of a bucking phenomenon induced by compressive strain.

A. Role of the interlayer material: comparison between transport properties of Al/Pt/Bi_2Te_3/Pt/Al and Al/Ti/Bi_2Te_3/Ti/Al

In our previous works[8,9], we have studied the transport properties of Al/Pt/Bi_2Se_3/Pt/Al and Al/Ti/Bi_2Se_3/Ti/Al where the flakes were exfoliated from single crystals. The comparison showed much larger critical current densities and $I_C R_N$ product for devices obtained with a Pt interlayer, both facts pointing towards a higher interface transparency barrier (I) (see Supplementary Figure 4), instrumental to observe Majorana bound state physics.

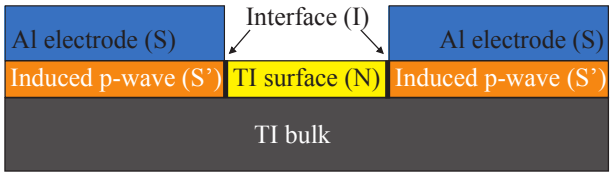

Supplementary Figure 4: **Cross section schematics of the effective device under consideration.** The transport properties can be assimilated to those of a S'INIS' Josephson junction where S' represent the induced chiral p-wave superconductor in the TI.

We have repeated this experiment on the Bi_2Te_3 flakes of this work, with the peculiar triangular morphology, by using a Ti interlayer.

Supplementary Table 1 summarizes the main transport properties of the junctions fabricated using both Pt and Ti. We confirm the general trend: the J_C and $I_C R_N$ values for the Pt interlayers are on average more than 5 times higher than those obtained with Ti. The same trend, higher values for Pt junctions, is observed for the average transparencies of the barrier I. This comparison is made at the first cool down.

	J_C (μA/μm)	$I_C R_N$ (μeV)	τ (transparency)
Rough flakes, **Pt** interlayer	2.7 ± 0.8	79 ± 19	0.67 ± 0.05
Rough flakes, **Ti** interlayer	0.41 ± 0.14	13 ± 3	0.49 ± 0.01

Supplementary Table 1: **Main parameters extracted from the IVCs of the Bi_2Te_3 junctions with different interlayer metals**.

Supplementary Figure 5 compares the conductance spectra, obtained by differentiating the current voltage characteristics (IVCs), of various junctions fabricated with Ti interlayer, with those obtained with a Pt interlayer. The curves of Supplementary Figure 5b (Ti interlayer) clearly show a dip at $V \approx 230\,\mu$eV that we have identified as $2\Delta_{S'}$, where $\Delta_{S'}$ is the induced gap into the TI[10,11]. In the spectra of Supplementary Figure 5b no other dips can be clearly identified. Supplementary Figure 5d shows instead various spectra relative to the IVCs of junctions fabricated with Pt interlayer. Also in this case we can identify a well developed dip at $V \approx 230\,\mu$eV (much more pronounced than the Ti case due to the higher transparency τ of the barrier I) that we correlate with $2\Delta_{S'}$, where again $\Delta_{S'}$ is the induced gap (this correlation is unambiguous because of the peculiar temperature dependence of $2\Delta_{S'}$[10,11]).

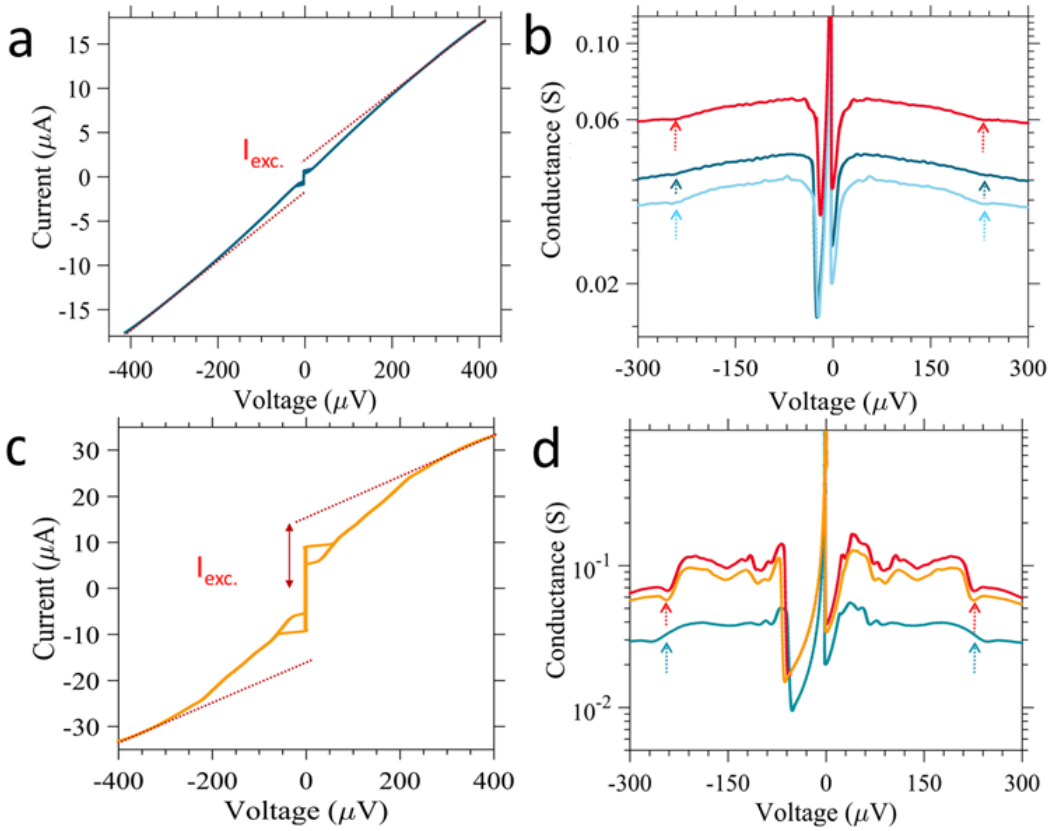

Supplementary Figure 5: **IVCs and conductance spectra for different interlayer metals.** IVCs of the Bi_2Te_3 junctions with (**a**) - Ti and (**c**) - Pt interlayer metal; the dashed line in both graphs represents linear fit to extract the excess current. Conductance spectra for three junctions with (**b**) - Ti and (**d**) - Pt interlayer metals; the arrows indicate the deeps corresponding to $2\Delta_{S'}$.

However the conductance curves of the junctions with Pt have many more dips at different voltages, associated to multiple Andreev reflections and that are made visible because of the higher

transparencies interfaces I, as we find in our experiment[11]. To summarize these measurements we observe 1) the interface Bi_2Te_3/Pt/Al and Bi_2Te_3/Ti/Al have the same transparency since the induced gap $\Delta_{S'} \approx 115\,\mu$eV is *exactly the same for both kind of junctions* and 2) the difference in the J_C values, $I_C R_N$ and transparency τ has to be related to the higher transparent interfaces I, between the part of the flake in the nano-channel and that under the electrodes, for the Pt junctions. The magnetic pattern of the Josephson current for both Pt and Ti junctions are Fraunhofer-like at the first cool down. However at the second cool down the junctions with Ti interlayer are not affected by the thermal cycle. The IVCs and the magnetic Fraunhofer pattern do not have any variation. We have cooled down the junctions from room to 20 mK temperature 3 times and the transport properties are completely preserved. This fact is in line with the results obtained by other groups working with 3DTI and using Ti as sticking layer.

What makes the junctions with Pt interlayers so different from the Ti?

We tend to exclude an origin related to a different chemistry between Pt and Ti while bonding to the Bi_2Te_3. This is because the values of the induces gap $\Delta_{S'}$ are identical, which is a consequence of very similar interface transparency.

Instead we will show that the completely different behavior between Ti and Pt junctions is related to different growth habits of the two metals on Bi_2Te_3.

Supplementary Figure 6a shows an AFM picture of a 3 nm Pt grown on a Bi_2Te_3 flake. The image shows a uniform layer that nicely wets the Bi_2Te_3 flake smoothening edges and corners. The growth habits of a 3 nm Ti film are instead quite different (see Supplementary Figure 6b). The Ti does not wet forming tiny grains (on average 20 nm in diameter) on the surface of Bi_2Te_3. As a result the morphology of the Al film, which grows on top of the Ti is much more granular (data not shown), compared to the growth on Pt.

The Al electrodes have the role of clamping the flake to the substrate so as to experience a tensile and compressive strain. For this to happen the Al and the flake underneath need to behave like almost the same material. The wetting properties of the Pt on the Bi_2Te_3 appear to promote an excellent Al adhesion and therefore an effective clamping of the flake to the substrate. The granular growth of the Ti interlayer on Bi_2Te_3 instead does not seem to be as effective in this respect. While the interface properties of the Al and Bi_2Te_3 through the Ti are very similar to the Pt junctions, the granularity of the Ti sticking layer makes the Al and the Bi_2Te_3 flake not as strongly connected to each other to behave as a homogenous materials. In this way no plastic

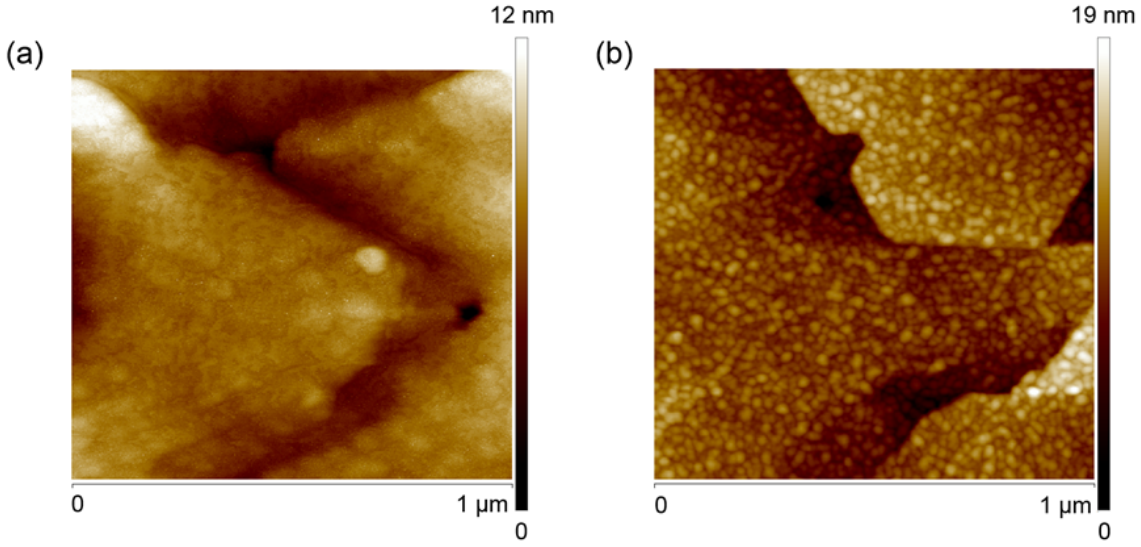

Supplementary Figure 6: **Growth habits of Pt and Ti on a Bi_2Te_3 flake.** AFM images of a Bi_2Te_3 flake covered (**a**) with 3 nm Pt and (**b**) with 3 nm Ti.

deformations are induced. Supplementary Figure 7b shows a typical top view SEM picture for one of the measured junction after several cool down; Supplementary Figure 7a is a SEM image of the same device taken with a tilted angle. None of the images show signature of buckling wave that instead we have detected in junctions with Pt interlayer.

It is worth mentioning what could be the origin of the much higher critical current densities we observe in junctions with Pt interlayer compared with those with Ti at the first cool down.

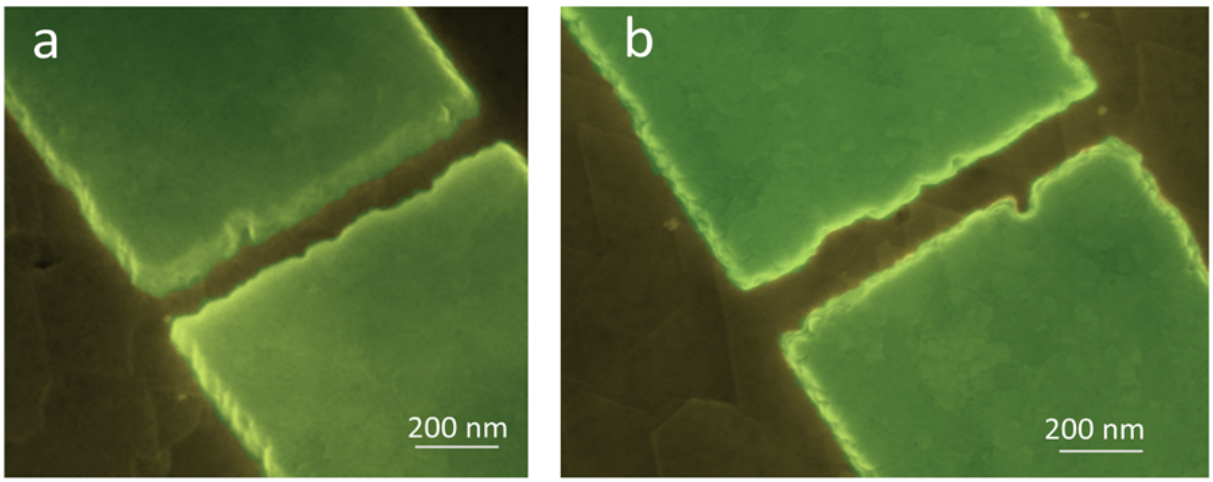

Supplementary Figure 7: **Colored SEM images for a junction with Al electrodes and Ti interlayer.** (**a**) Tilted view; (**b**) side view. The electrodes are represented in light green color.

We believe it is a consequence of the occurrence of a tensile strain experienced by the flake in the nanogap.

The origin of the barrier I between the flake under the Al/Pt(Ti) electrodes and the one in the nanogap is not clearly established. One can possibly expect some doping from the metal, which shifts the Fermi energy of the flake under the electrode, compared to the one in the nanogap. The occurrence of a tensile strain at the nanogap while cooling the nanodevice, shift the Dirac point toward the valence bands making it more doped. Since the effect of strain is much more dominant in junctions with Pt, one can expect a better Fermi level matching between the two parts of the flake, under the electrodes and at the nanogap, resulting in a higher transparency barrier and higher J_C values.

Supplementary Note 4. TWO DIMENSIONAL MAGNETO-FINGERPRINTS IN Bi_2Te_3 CHANNELS

In the paper by Kandala et al.[12], the authors study the magneto transport of Bi_2Se_3 channels, where the films have a typical growth with pyramidal domains. The authors reveal signatures of Aharonov-Bohm (AB) orbits, manifesting as periodic magneto conductance fluctuations. The length scale of the orbits corresponds to the typical perimeter of triangular terraces found on the surface of these thin film devices. They conclude that the periodic magneto-fingerprint arises from coherent scattering of electron waves from the step-edges. To demonstrate that this scenario is also valid for the Bi_2Te_3 flakes, used in our work, we have preformed magneto transport measurements down to 20 mK temperature on devices with a Hall configuration.

Supplementary Figure 8a shows the longitudinal resistance between the two voltage probes with a distance of 0.5 μm (the classical quadratic magneto-resistance background has been subtracted for clarity) in the range of magnetic field 1-3 T for various temperatures. From the Fourier transform of the curves, Supplementary Figure 8b, we clearly observe a peak around 2.9 T^{-1} which corresponds to an area of 0.012 μm^2 in line with the morphology of our flakes and in complete agreement with the values reported in Ref. 12 for a device of similar dimensions as ours. Moreover we clearly see that the amplitude of the magnetoresistance oscillations decreases with temperature (inset of Supplementary Figure 8b) in a similar fashion as in Ref. 12. This strongly suggests that also in our case the periodic magneto-resistance oscillations arise from coherent scattering of electron wave from the corners and/or step-edges where two pyramidal domains merge.

It is also worth discussing if one can find any apparent correlation, between the orientation of the

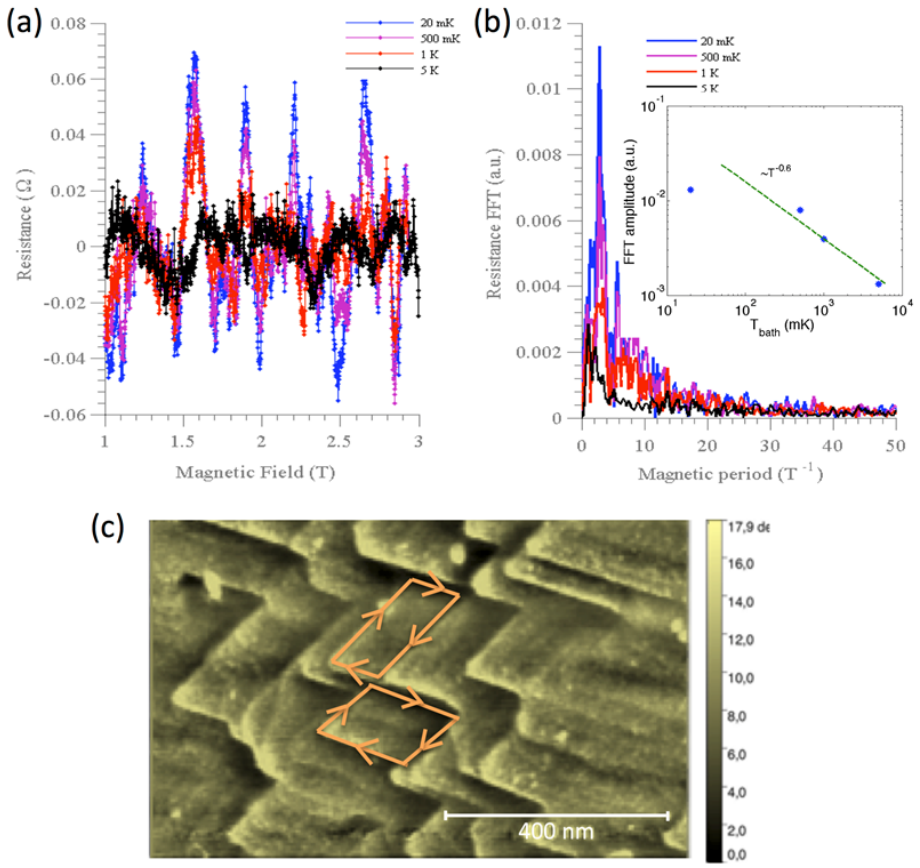

Supplementary Figure 8: **Two dimensional magneto-fingerprints in Bi_2Se_3 channels.** (**a**) Longitudinal resistance as a function of magnetic field for a channel length of 0.5 μm at different temperatures. (**b**) Fourier transform of the curves of panel (a). The inset shows the Fourier transform amplitude at 2.9 T^{-1} as a function of temperature. The data have a typical power law dependence (with exponent -0.6). (**c**) Typical surface morphology of the flakes used in the experiment. The orange lines delimitate two possible Arhonov-Bhom orbits with approximately the same area.

nano-pyramidal domains and that of the electrodes, with the occurrence of unconventional magnetic field pattern related to 0 and π trajectories inside the Bi_2Te_3 nanochannel. We have investigated by SEM all the junctions having a 0-π transition and we do not find any clear correlation between the orientation of the nano-pyramidal domains and that of the electrodes. However this is not surprising if one considers that the basic mechanism to get an inverted magnetic field pattern, with a minimum of the critical current at zero external field, is the occurrence of 0 and π facets within the same nanogap. In our flakes the occurrence of AB oscillations supports preferential trajectories of electrons and holes along the edges of the triangles. Supplementary Figure 9 shows

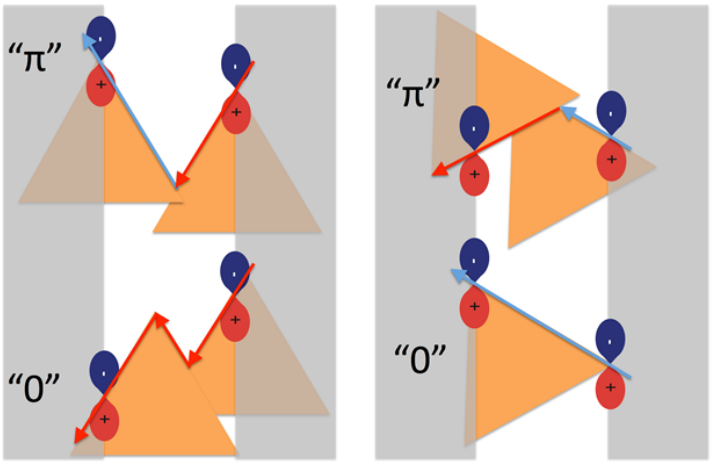

Supplementary Figure 9: **Schematic pictures of a Josephson junction with different orientation of the pyramidal domains in the nanogap with respect to the Al electrodes.** In the left panel, the main direction of the pyramidal domains is aligned parallel to the Al electrodes, while it is perpendicular to them in the right panel. In the figure, 0 and π trajectories can be found in both cases.

a sketch corresponding to two extremes cases where the main alignment direction of the pyramidal domains is parallel (Supplementary Figure 9a) or perpendicular (Supplementary Figure 9b) to the electrodes. We see that in both cases one can find 0 and π trajectories, which would lead to an inverted Fraunhofer pattern.

Supplementary Note 5. PERIODICITY OF A MAGNETIC PATTERN WITH REGULAR AND RANDOM DISTRIBUTED 0-π FACETS.

The magnetic patter of a regular 0-π faceted Josephson junction is strongly modified compared to a Fraunhofer-like. Supplementary Figure 10 shows the $I_C(B)$ for a junction formed by a total of 10 equal in size 0 and π facets carrying the same current[17]. The absolute maximum of the pattern is found at $5\phi_0$. This is quite easy to understand since one requires a ϕ_0 to reverse the phase sign of every π facet. However one can still find the periodicity connected to the total junction's width in the position of the minima which happen at multiple of ϕ_0 (see Supplementary Figure 10). For a random distribution of facets the absolute maximum will always occur at finite field (which will depend on the microscopic distribution of 0-π facets), while at zero external field one can find a local maximum (not the absolute maximum) or a local minimum again dependent on the details of the facets microscopic distribution.

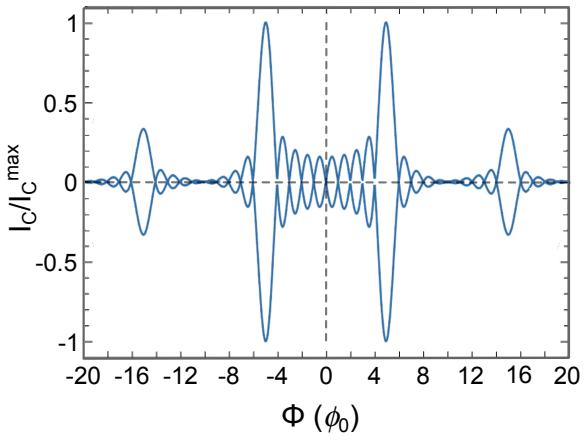

Supplementary Figure 10: **Simulated magnetic flux dependence of the Josephson current for an array of 10 alternating 0 and π facets.**

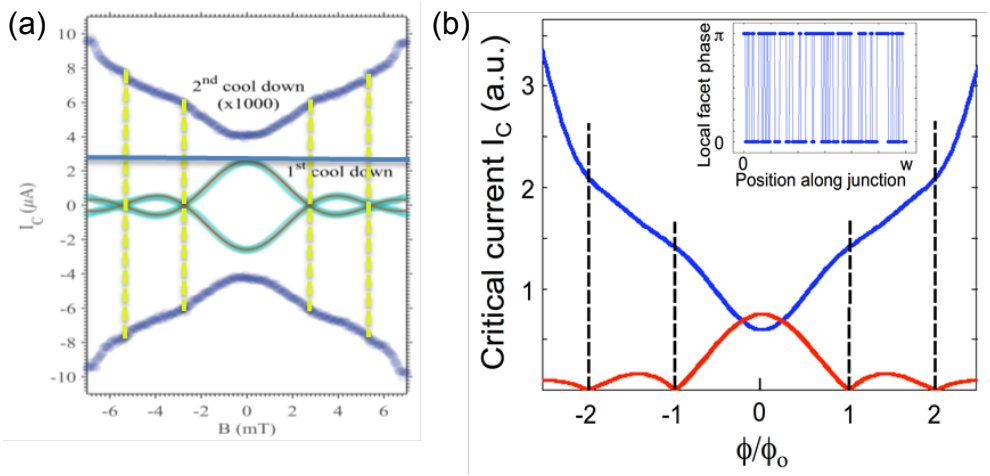

Supplementary Figure 11: **Magnetic field dependence of a typical Bi_2Te_3 junction compared with that of a simulated array of random distributed 0 and π facets.** (**a**) Critical current I_C dependence on the externally applied magnetic field B for one of our junctions at 20 mK, before (cyan) and after (blue) the thermal cycle. At the first cool down the $I_C(B)$ dependence shows a conventional Fraunhofer dependence. After the thermal cycle (blue points), the critical current is dramatically reduced (the data points are multiplied by a factor 1000 for clarity), and a dip at B=0 appears. (**b**) Numerically calculated $I_C(B)$ (blue curve) for a random distribution of 0 and π facets (see inset) compared with a conventional Fraunhofer type dependence calculated considering a uniform current distribution.

The periodicity connected to the size of the junction can be still identified as local minima, local maxima or change in slope in the $I_C(B)$. As an example in Supplementary Figure 11(b) we show the computed magnetic field dependence $I_C(B)$ for a uniform current distribution (red curve) compared with a random distribution of 0 and π facets (blue curve).

For the random case we can clearly identify change of slopes at ϕ_0 and $2\phi_0$ (indicated by the dashed lines) which corresponds to the periodicity determined by the width of the junction. Indeed such a scenario qualitatively reproduces what we observe in our experiment (see Supplementary Figure 11(a)) and that is discussed in the manuscript.

Supplementary Note 6. FIT OF THE $I_C(T)$ DEPENDENCE WITH A SINIS MODEL

The full theory of the Josephson effect in SINIS structures with chiral p-wave ($p_x + ip_y$) superconducting leads is still lacking. In Ref. 13, Sawa et al have considered a SINIS system with $p_x + ip_y$ superconducting leads and diffusive normal part, numerically solved Usadel equations and determined the $I_C(T)$ dependence. This dependence turns out to be qualitatively very similar to that of an usual SINIS junction with s-wave leads. Moreover, in the limit of highly transparent insulating barriers $I_C(T)$ dependence for s-wave and p-wave leads are found to be essentially identical. In Ref. 14 the authors have considered a SINIS structure with chiral p-wave leads and short ballistic normal metal. These authors have also found that for perfectly transmitting barriers both $p_x + ip_y$ and s-wave pairing symmetries lead to the same $I_C(T)$ dependence. In view of these previous works, we have modeled our highly transparent junctions measured during the first cool down as S'INIS' structures (where S' is the proximity induced superconductor) with conventional s-wave superconducting leads, for which a simple analytical formula for the Josephson current exists in the clean ballistic limit[15]. The same approach has been adopted in an earlier work[16].

For our S'INIS' junctions, we consider the limit of wide junction, $k_F w \gg 1$, and use the following expression for the critical current

$$I_J(\phi) = \frac{4ek_BT}{\hbar}\frac{k_F w}{\pi}\sin\phi \sum_{\omega_n>0}\int_0^1 d\mu \frac{t_1 t_2}{\sqrt{Q\left(\phi, \sqrt{1-\mu^2}\right)}} \,. \tag{5}$$

Here $\mu = \sin\theta$, where θ is the angle between the velocity of an electron flying out of a lead and the shortest line connecting the two leads,

$$t_1 = \frac{D_1}{2-D_1} \,, \qquad t_2 = \frac{D_2}{2-D_2} \tag{6}$$

are the effective Andreev transparencies of the barriers[16], D_1 and D_2 are the usual barrier transparencies in the normal state. In Eq. (5), the function Q is defined as

$$Q\left(\phi,\sqrt{1-\mu^2}\right)=\left[t_1t_2\cos\phi+\left(1+(1+t_1t_2)\frac{\hbar^2\omega_n^2}{\Delta^2}\right)\cosh\left[2\omega_n t_0(\mu)\right]+\right.$$
$$\left.+(t_1+t_2)\frac{\hbar^2\Omega_n\omega_n}{\Delta^2}\sinh\left[2\omega_n t_0(\mu)\right]\right]^2-(1-t_1^2)(1-t_2^2)\frac{\hbar^4\Omega_n^4}{\Delta^4}\ , \tag{7}$$

$$\omega_n=\frac{\pi k_{\mathrm{B}}T(2n+1)}{\hbar}\ , \tag{8}$$

$$\hbar\Omega_n=\sqrt{\hbar^2\omega_n^2+\Delta^2}\ , \tag{9}$$

ω_n are the Matsubara frequencies, and $t_0(\mu)$ is the angular dependent average flight time of an electron between the leads for a given Fermi speed v_{F}, mean free path l_{e}, the separation between the leads L, and

$$t_0(\mu)=\frac{l_e}{(1-\mu^2)v_{\mathrm{F}}\left(\sqrt{1+\frac{l_{\mathrm{e}}^2}{L^2(1-\mu^2)}}-1\right)}\ . \tag{10}$$

Supplementary Equation (10) may be viewed as an interpolation between the clean limit ($l_{\mathrm{e}}\gg L$), in which case

$$t_0(\mu)=\frac{L}{v_{\mathrm{F}}\sqrt{1-\mu^2}}\ , \tag{11}$$

and the diffusive limit ($l_{\mathrm{e}}\ll L$) , where t_0 does not any more depend on the angle and reads

$$t_0=\frac{2L^2}{v_{\mathrm{F}}l_{\mathrm{e}}}\ . \tag{12}$$

For the normal state resistance in this model we find

$$\frac{1}{R}=\frac{e^2}{\pi\hbar}\frac{k_{\mathrm{F}}w}{\pi}\frac{1}{\frac{1}{D_1}+\frac{1}{D_2}-1+\frac{2L}{\pi l_{\mathrm{e}}}}\ . \tag{13}$$

The model outlined above differs from the original one[15] in two ways. Since we are dealing with a two dimensional normal layer (while in Ref. 15 a three dimensional normal metal was considered), we have replaced the integral over the two transverse components of the wave vector, k_y and k_z, by the corresponding one-dimensional integral over k_y, i.e. we have replaced $dk_ydk_z/(2\pi)^2$ by $dk_y/2\pi h$, where h is the flake thickness. Second, we have introduced finite mean free path into the expression for the Josephson current in a phenomenological way.

Namely, we have replaced the ballistic expression for the flight time, Supplementary Equation (11), by a more complicated one containing the mean free path, Supplementary Equation (10). We

have verified that this replacement correctly reproduces the known expression for the Josephson current of a short diffusive SINIS junction.

We have performed a fit on a selection of the junction listed in Table 1 (see main text), which covered a wide range in the magnitude of the critical current values (see Supplementary Figure 12). We used a value for the S' superconducting gap of $\Delta_{S'} \approx 125\,\mu$eV, which is close to the value of the Al superconducting gap. The Fermi velocity of the electrons has be chosen to be $v_F = 3.5 \cdot 10^5$

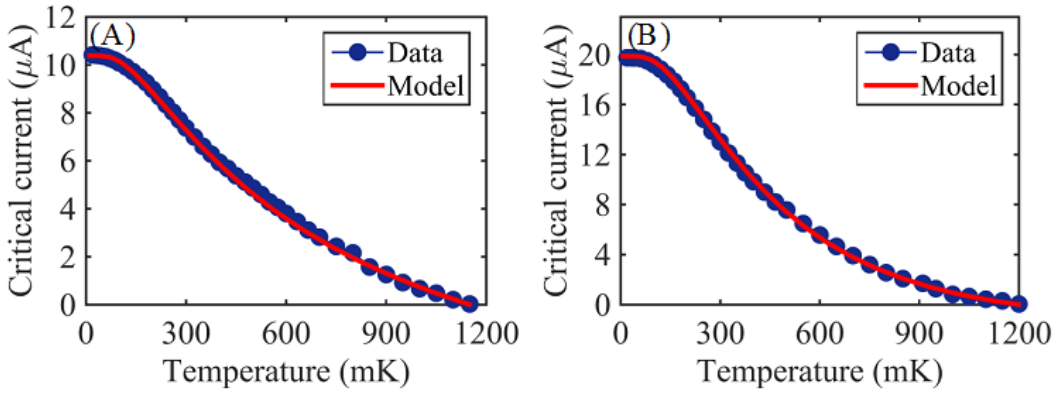

Supplementary Figure 12: **Critical current as a function of the temperature at the first cool down.** The measured $I_C(T)$ dependencies are for samples MS1 (panel **A**) and FS4 (panel **B**). The red line is the best fit, considering a quasi-ballistic model (Supplementary Equations (5) and (7)). The fit parameters are listed in Supplementary Table 2.

m s^{-1}, in agreement with literature, and the fitting parameters are: the Fermi energy, E_F, the mean free path, l_e, and the transparencies of the barriers, which we assumed to be identical, $D_1 = D_2 = D$. The theoretical value of the normal state resistance, R_{th}, has been determined from Supplementary Equation (13) and the Thouless energy was estimated as $E_{Th} = h v_F l_e / L^2$.

The extracted values of the mean free path (l_e) are typically comparable to the junction length, thus confirming a picture of an intermediate, between ballistic and diffusive, transport regime. The scattering centers are probably the edges of the pyramidal domains of the film, as we have discussed in the main text.

It is known[16] that the bulk of the flake should behave as a resistive shunt. From the expression

$$\frac{1}{R_{sh}} = \frac{1}{R_{exp}} - \frac{1}{R_{th}} \tag{14}$$

we have extracted the effective shunt resistances of the devices. In Supplementary Equation (14) R_{th} is the prediction of Supplementary Equation (13) and R_{exp} is the resistance measured in the experiment. The sheet resistances of the films associated with the bulk transport, $R_\square = R_{sh} w/L$,

vary in the range between 150 and 550 $\Omega/\square$. The corresponding resistivities, defined as $\rho = R_\square h$, are shown in Supplementary Table 2 and change between 1000 and 5000 $\mu\Omega$cm, which is about one order of magnitude larger than the bulk resistivity reported in Ref. 16, which probably indicates a lower level of doping in our material. We believe that the scattering of the extracted values of the bulk resistivity between different devices is mostly caused by the uncertainty in the geometry of the samples, but it may also be explained by slightly different levels of doping.

Device	l_e (nm)	D	E_F (meV)	E_{Th} (μeV)	R_N^{th} (Ω)	R_{sh} (Ω)	$R_\square$ (Ω)	ρ ($\mu\Omega$cm)
JM1	140	.99	106	363	566	101	152	1200
JM10	130	.98	140	341	134	47	236	1900
SM4	100	.98	172	954	45	27	543	4300
SM1	95	.98	213	920	37	25	502	4000
SF4	35	.94	210	392	22	3.5	209	1670

Supplementary Table 2: **Parameters extracted from the fit of the $I_C(T)$**. The mean free path l_e, the transparency of the barriers D (assuming the two barriers are identical) and the Fermi energy E_F are the free parameters of the fit. From these parameters we derived the Thouless energy E_{Th}, the expected resistance above the gap R_N^{th}, the calculated shunt resistance of the flake R_{sh}, and the corresponding sheet resistance $R_\square$ and resistivity ρ. The induced gap at zero temperature was taken to be $\Delta(0) = 125\,\mu$eV and at higher temperatures the standard BCS gap temperature dependence has been used.

SUPPLEMENTARY REFERENCES

[1] Rosenthal, P. A., Beasley, M. R., Char, K., Colclough, M. S. & Zaharchuk, G. Flux focusing effects in planar thin-film grain-boundary Josephson junctions. *Appl. Phys. Lett.* **59**, 3482 (1991).

[2] Romijn, J., Klapwijk, T. M., Renne, M. J. & Mooij, J. E. Critical pair-breaking current in superconducting aluminum strips far below T_c. *Phys. Rev. B* **26**, 3648-3655 (1982).

[3] Liu, W. et al. Anisotropic interactions and strain-induced topological phase transition in Sb_2Se_3 and Bi_2Se_3. *Phys. Rev. B* **84**, 245105 (2011).

[4] Young, S. M. et al. Theoretical investigation of the evolution of the topological phase of Bi_2Se_3 under mechanical strain. *Phys. Rev. B* **84**, 085106 (2011).

[5] Zeljkovic, I. et al. Strain engineering Dirac surface states in heteroepitaxial topological crystalline insulator thin films. *Nat. Nanotechnol.* **10**, 849-853 (2015).

[6] Liu, Y. et al. Tuning Dirac states by strain in the topological insulator Bi_2Se_3. *Nature Phys.* **10**, 294-299 (2014).

[7] Bowden, N., Brittain, S., Evans, A. G., Hutchinson, J. W., & Whitesides, G. M. Spontaneous formation of ordered structures in thin films of metals supported on an elastomeric polymer. *Nature* **393**, 146-149 (1998).

[8] Galletti, L. et al. Influence of topological edge states on the properties of $Al/Bi_2Se_3/Al$ hybrid Josephson devices. *Phys. Rev. B* **89**, 134512 (2014).

[9] Galletti, L. et al. Josephson effect in $Al/Bi_2Se_3/Al$ coplanar hybrid devices. *Physica C* **503**, 162 (2014).

[10] Kjaergaard, M. et al. Transparent Semiconductor-Superconductor Interface and Induced Gap in an Epitaxial Heterostructure Josephson Junction. *arXiv:1607.04164v2* (2016)

[11] Galletti, L. et al. High-Transparency Al/Bi_2Te_3 Double-Barrier Heterostructures. *IEEE Trans. Appl. Supercond.* **27**, 1-4 (2017).

[12] Kandala, A., Richardella, A., Zhang, D., Flanagan, T. C., & Samarth, N. Surface-sensitive two-dimensional magneto-fingerprint in mesoscopic Bi_2Se_3 channels. *Nano Lett.* **13**, 2471-2476 (2013).

[13] Sawa, Y., Yokoyama, T., Tanaka, Y. & Golubov, A. A. Quasiclassical Green's function theory of the Josephson effect in chiral p-wave superconductor/diffusive normal metal/chiral p-wave superconductor junctions. *Phys. Rev. B* **75**, 134508 (2007).

[14] Tkachov, G. & Hankiewicz, E. M. Helical Andreev bound states and superconducting Klein tunneling in topological insulator Josephson junctions. *Phys. Rev. B* **88**, 075401 (2013).

[15] Galaktionov, A. V. & Zaikin, A. D. Quantum interference and supercurrent in multiple-barrier proximity structures. *Phys. Rev. B* **65**, 184507 (2002).

[16] Veldhorst, M. et al. Josephson supercurrent through a topological insulator surface state. *Nat. Mater.* **11**, 417-421 (2012).

[17] Smilde, H. J. H. et al. d-Wave-Induced Josephson Current Counterflow in $YBa_2Cu_3O_7$/Nb Zigzag Junctions. *Phys. Rev. Lett.* **88**, 057004 (2002).